Journal Article

Low velocity oblique impact behaviour of glass, carbon and aramid fibre reinforced polymer laminates

Banhart, D., Monir, S., Jones, M., Luhyna, N., Day, R.J., and Vagapov, Y.

Mechanics of Advanced Materials and Structures

ISSN: (Print) (Online) Journal homepage: www.tandfonline.com/journals/umcm20

Low velocity oblique impact behaviour of glass, carbon and aramid fibre reinforced polymer laminates

Dirk Banhart, Shafiul Monir, Martyn Jones, Nataliia Luhyna, Richard J. Day & Yuriy Vagapov

To cite this article: Dirk Banhart, Shafiul Monir, Martyn Jones, Nataliia Luhyna, Richard J. Day & Yuriy Vagapov (18 Mar 2025): Low velocity oblique impact behaviour of glass, carbon and aramid fibre reinforced polymer laminates, Mechanics of Advanced Materials and Structures, DOI: 10.1080/15376494.2025.2477808

To link to this article: https://doi.org/10.1080/15376494.2025.2477808

Published online: 18 Mar 2025.

MECHANICS OF ADVANCED MATERIALS AND STRUCTURES
https://doi.org/10.1080/15376494.2025.2477808

Taylor & Francis
Taylor & Francis Group

ORIGINAL ARTICLE

OPEN ACCESS Check for updates

Low velocity oblique impact behaviour of glass, carbon and aramid fibre reinforced polymer laminates

Dirk Banhart, Shafiul Monir, Martyn Jones, Nataliia Luhyna, Richard J. Day, and Yuriy Vagapov

Faculty of Arts, Computing and Engineering, Wrexham University, Wrexham, UK

ABSTRACT
This paper provides a numerical comparative analysis of the low-velocity oblique impact performance of glass, carbon and aramid fiber reinforced polymer laminates with different quasi-isotropic and symmetric stacking sequences. To ensure accuracy of simulation results, the numerical model was validated using previously published experimental data. Puck failure criterion was applied for both the validation case and the numerical results' evaluation and benchmarking. The results shown that, within the oblique impact angles from 0° to 60°, the most critical angles produced damage are 25° and above 55°. ANSYS Composite PrepPost + Transient Structural software was used for numerical setup and simulation.

ARTICLE HISTORY
Received 2 December 2024
Accepted 6 March 2025

KEYWORDS
Composite laminate; drop-weight impact test; low velocity; oblique impact; implicit FEM; ANSYS ACP; transient structural

1. Introduction

Composite materials are widely used in high performance mechanical applications to significantly reduce mass of components and improve structural strength due to their advanced physical properties and lightweight nature [1]. Today, composite materials are in high demand for mechanical and structural manufacturing across the aerospace [2], automotive [3], marine [4] and civil engineering industries [5]. However, in these applications, composite materials are exposed to various hazards, including low- and high-velocity impacts. High-velocity impacts often result in damage such as penetration or perforation of the composite material [6], while low-velocity impacts can lead to either clearly visible impact damage (CVID) or barely visible impact damage (BVID) [7], with BVID being the more common case [8,9]. Delamination between plies occurring under BVID is often invisible on the component surface [10]. This leaves the composite material in a weakened state, where its compressive strength is significantly reduced [11], potentially leading to structural failure of the composite material with possibly fatal consequences. Therefore, a thorough understanding and analysis of composite material performance under such conditions is crucial. For this purpose, the drop-weight impact test is intensively used as an efficient, standardized method for investigating low-velocity impact behavior and conducting damage material analysis [12,13].

In engineering and research practice, the analysis of composite laminate plates using drop-weight impact tests has attracted significant attention for studying material performance and predicting the occurrence of delamination and faults. Many research reports on this subject combine both experimental and numerical methods, with practical tests often used to validate simulation. For example, Alomari et al. [14] conducted an investigation involving both experimental and computational analyses to assess the response of carbon fiber reinforced polymer (CFRP), glass fiber reinforced polymer (GFRP), and hybrid fiber composite plates under low-velocity impact. The tests discussed in [14] were performed in accordance with ASTM D7136/D7136M standard. The impact behavior of the composite laminate plates was evaluated by measuring the energy absorbed by the samples during the impact events. Using ANSYS LS-DYNA, the study examined the influence of various factors, such as stacking sequence, number of plies, and individual ply thickness, on energy absorption characteristics. Research findings demonstrated that the CFRP laminate plate exhibited significantly superior impact resistance compared to the GFRP laminate plate. This difference in impact resistance was attributed to the CFRP's ability to absorb higher levels of energy during impact events. Additionally, the simulations showed that the stacking sequence [90/0/45/−45]s outperformed the [60/45/−45/−60]s configuration in terms of impact resistance.

Gliszczynski [15] conducted an in-depth study of the low-velocity impact behavior of GFRP laminate plates with quasi-isotropic stacking sequences. The study combined both experimental testing, following ASTM D7136/D7136M guidelines, and numerical simulations using an implicit transient analysis performed within the ANSYS software package. Notably, a high level of correlation between the numerical and experimental results was achieved, confirming the satisfactory accuracy of the numerical approach. In this study [15], the Hashin criterion was applied to predict areas of fiber failure and matrix failure. Specifically, the criterion provided a valid estimate of fiber failure but tended to

CONTACT Yuriy Vagapov y.vagapov@glyndwr.ac.uk Faculty of Arts, Computing and Engineering, Wrexham University, Wrexham, UK.

overestimate areas of matrix failure. Three distinct numerical models (SHELL, SOLSH, and SOLID) were evaluated, with the SOLID model demonstrating the highest consistency with the experimental results. This accurate numerical model serves as a valuable tool for further investigation and analysis of GFRP laminate plates built using quasi-isotropic stacking sequences under low-velocity impacts. The alignment between the experimental and numerical findings enhances understanding of the composite material's response to impact, aiding in the development and design of composite structures having advanced impact-resistant properties.

The performance of CFRP thick composite laminate plates under low-velocity impacts was investigated by Gonzalez-Jimenez et al. [16] using both numerical modeling and experimental testing techniques. The study utilized LS-DYNA with the MAT54 material model based on the Chang-Chang failure criterion. The experimental tests were conducted following ASTM D7136/D7136M standards. Research findings demonstrated a high level of agreement between numerical and experimental results in terms of delamination prediction. The numerical model also showed good accuracy in predicting the maximum contact force and the total energy absorbed by the composite laminate sample during impact events. However, the model did not provide satisfactory quantitative accuracy in predicting the strain values observed in the experiments. Despite this limitation, the model still provided reasonable predictions.

Perillo et al. [17] examined the damage progression in stitch-bonded GFRP composite laminate plates subjected to low-velocity impacts, employing both experimental and numerical approaches. The experimental drop-weight impact tests were conducted in accordance with the ASTM D7136/D7136M guidelines. For numerical simulations, ABAQUS/Explicit was employed, with composite material modeling performed using VUMAT. The numerical model incorporated Puck and Hashin failure criteria for damage assessment. Using independently obtained material data, the model successfully predicted the impact performance of the composite laminate plates for various energy levels and stacking sequences. Complete damage of the composite material in the form of matrix cracking, delamination, and fiber failure, was observed for the expected increase in the impact energy.

However, the numerical and analytical methods (without practical experiments and tests) used for composite material performance analysis are highly attractive to avoid testing hardware implementation and, therefore, to reduce the overall time and cost of research [18,19]. A numerical simulation verified in terms of result accuracy can provide a rapid and comprehensive insight into material behavior under a wide range of operational and structural conditions. For example, a simulation-based approach was used by Bozkurt et al. [20] to study a drop-weight impact test applied to composite laminate plates. The simulation utilized ABAQUS/Explicit as the FEM solver. To accurately simulate ply damage, a continuum damage mechanic-based damage model was implemented in VUMAT. The damage leading to delamination was effectively modeled using cohesive elements with varying orientations incorporated in the interfaces of plies. Research findings indicated that during the low-velocity impact event, the primary failure mechanism involves matrix cracking occurring in the lowermost plies. This failure is independent of the stacking sequence of the composite laminate plate. In addition, the numerical model simulations successfully predicted the expansion of the delamination areas predominantly occurring in alignment with the fiber direction of the lower adjacent ply. This failure mechanism is consistent with the concept of bending stiffness mismatching.

An oblique low-velocity impact is the most common hazard affecting the structure of the composite material operating in a harsh environment. This is particularly relevant to the advanced application of composite materials in aerospace, marine and transport applications where the reliability of composite details is crucial. Therefore, numerical analyses of material performance under low-velocity oblique impact are of particular interest as it can provide results relevant to the realistic behavior and fault prediction of composites under BVID conditions. A detailed numerical analysis using ABAQUS/Explicit is provided by Zhao and Zou [21] where authors investigated unidirectional CFRP behavior under low-velocity impacts including normal and oblique directions. The simulation focused on the damage of the material subjected to multiple low-velocity impacts under normal and different impact angles. The results show that the energy absorption and material damage produced by the normal impact is larger than in comparison to the oblique impact. The increase in oblique impact angle between the impactor and sample plane makes the contact force higher and the material damage more critical.

Mao et al. [22] reported on the dynamic response and damage behavior of fiber reinforced composite laminate plates subjected to low-velocity oblique impact. This study was conducted using both analytical and numerical investigations. ABAQUS/Explicit was employed as a numerical tool for simulations. The research revealed that, under oblique impact conditions, composite laminate plates are more susceptible to matrix damage due to the presence of shear forces during oblique contact. Furthermore, the damage profile observed in composite laminate plates under oblique impact differed significantly from that seen in normal impact events. The dynamic response of the composite laminate plates under oblique impact also showed considerable variation when compared to responses under normal impact conditions.

Experimental and numerical approaches were applied for low-velocity impact analysis in [23] where CFRP laminates were subjected to various normal and oblique impact energies. It was found that delamination damage of CFRP samples under oblique impact conditions mainly corresponds to the energy absorption properties. Whereas the energy absorption performance depends on the peak force, sample thickness and angle of the oblique impact. Similar results were obtained by Zhang et al. [24] conducted analytical and numerical analysis of rectangular samples of composite laminates subjected to low-velocity oblique impacts. It was shown that impact contact time and reflection time depend on the size and thickness of the composite sample as well as the radius of the impactor.

A numerical investigation by Rawat et al. [25] analyzed the influence of oblique impact on GFRP composite laminates. The study utilized the LS-DYNA explicit FEM solver and HyperMesh for composite material modeling. The numerical results from the impact modeling revealed that the impact angle significantly affects the response of the composite laminate plate to oblique impacts. This finding has important implications for the design of mechanical components exposed to oblique, low-velocity impact scenarios. The research further showed that the impact energy absorbed by the GFRP laminate plates is enlarged following the increase in the inclination angle, but only up to a certain critical angle. Beyond this critical angle, energy absorption begins to decrease.

Sun et al. [26] conducted an extensive numerical study on the oblique low-velocity impact response and damage behavior of CFRP laminate plates, specifically examining the effect of impact angle. The study employed ABAQUS/Explicit for the numerical simulations. The research findings demonstrated that as the impact angle increases, the influence of tangential force becomes more pronounced. Consequently, energy absorption gradually shifts from normal plastic deformation to tangential deformation and friction. This mechanism increases the energy dissipation due to a relatively longer duration of contact and larger displacement of the impactor. Regarding delamination damage, the upper plies of the composite laminate plates were significantly affected by tangential loads, with damage intensifying as the impact angle increased. In contrast, the delamination damage in the lower plies was primarily influenced by normal loads, which weakened as the impact angle increased. Additionally, the damaged area at the top interface expanded by 132.1% from 0° to 60° impact angle, while the damaged area at the lowest interface decreased by 36.6%, indicating a reduction with increasing impact angle.

The presented study contributes to an extensive analysis of the low-velocity impact behavior of GFRP, CFRP, and aramid fiber reinforced polymer (AFRP) laminate plates having different quasi-isotropic and symmetric stacking sequences subjected to a range of oblique impacts. The composite materials (GFRP, CFRP, and AFRP) were numerically investigated under the same impact conditions to enable a comparative analysis. Unlike most published reports on numerical research of material impact performance, this study utilizes ANSYS Composite PrepPost + Transient Structural and demonstrates that this software is a suitable and effective tool for numerical impact research. To ensure the accuracy of the numerical simulation, a validation case was conducted in which the numerically predicted delamination areas at various impact energies were compared with the experimental results provided by Falco et al. [27], establishing a correlation of accuracy. In this study, the Puck failure criterion was employed for the validation case and for evaluating and benchmarking results.

The ultimate material strengths required for the numerical analysis of the composites were obtained from various published sources, which were then used to calculate the orthotropic material properties of the resulting composite laminates. A virtual model of the drop-weight impact test setup, including the impactor, test specimens, and support, was created to analyze the impact performance from different angles. A numerical validation case was performed to assess the correlation between experimental and numerical results, with the assumption that if the correlation is satisfactory, subsequent simulation results would be reliable.

After validation, the proposed virtual model was used to perform a series of simulations to investigate the influence of laminate stacking sequences on composite impact resistance under low-velocity oblique impacts at various impact angles. The simulations also examined the kinetic energy, X- and Y-components of contact forces during impact, total deformation, von Mises stresses, Puck failure, and delamination areas of the composite laminates. The results obtained from numerical simulations were evaluated and compared based on the types of composite material, the influence of stacking sequence on impact behavior, and damage analysis of the laminate plates as well as individual plies. Based on the findings and discussion, insights and recommendations for the design using composite laminates are formulated. In composite component design, a comprehensive understanding of low-velocity oblique impact and damage behavior helps mitigate damage that could lead to catastrophic failure due to material weakening, enabling a more economical design which maintains sufficient impact resistance.

2. Drop-weight impact test setup

The drop-weight impact test according to the ASTM D7136/D7136M standard [28] was used as a basis for the impact performance investigation. This test is the standard method for testing and measuring the resistance to damage that is widely applied to fiber reinforced polymer matrix. The setup of the drop-weight impact test is shown in Figure 1. However, four rubber pins, which press the test specimen down onto the support, have been omitted for simplification. The dimensions of the setup are shown in Table 1.

In addition to different impact velocities and angles of impact, six different stacking sequences were tested for the composite laminate test specimen (listed in Table 2). All stacking sequences exhibit quasi-isotropic behavior and are even symmetric. Six stacking sequences selected for analysis are arranged in a way to provide equal strength performance of the material in each direction of loading (in-plane). The rationale behind these choices is to evaluate how different fiber orientations influence impact resistance and damage propagation.

3. Governing equations

The following governing equations provided in this section were utilized to dimension the drop-weight test setup, to calculate the orthotropic material properties of

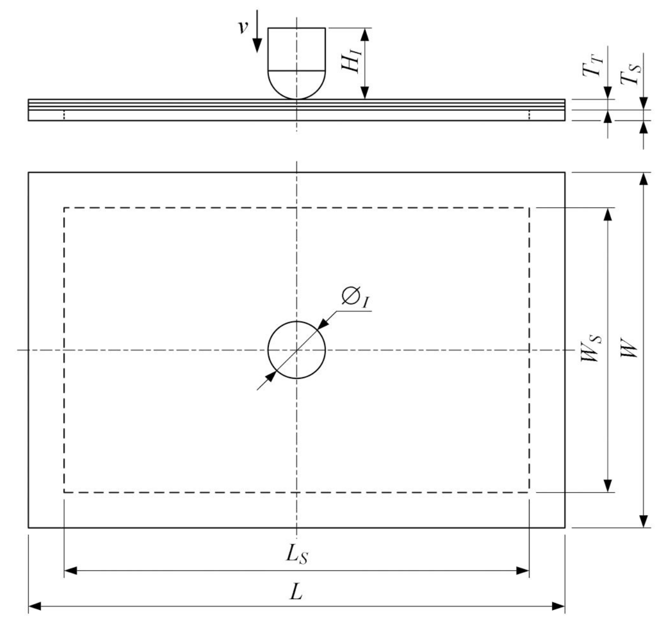

Figure 1. Schematic of the drop-weight impact test setup.

Table 1. Dimensions of drop-weight impact tests.

Dimension	Symbol	Value
Impactor diameter	$Ø_I$	16 mm
Impactor height	H_I	18 mm
Test setup length	L	150 mm
Test setup width	W	100 mm
Support cutout length	L_S	125 mm
Support cutout width	W_S	75 mm
Support thickness	T_S	3.0 mm
Test specimen thickness	T_T	2.944 mm
Ply thickness	–	0.184 mm
Number of plies	–	16
Impactor mass	–	5.5 kg
Impactor velocity	v	1.907 m/s; 2.335 m/s
Angle of impact	–	0°–60° (steps of 5°)

Table 2. Quasi-isotropic stacking sequences.

Designation	Stacking Sequence
QI-I	[22.5/−22.5/67.5/−67.5/0/45/−45/90]s
QI-II	[22.5/−22.5/45/−45/67.5/−67.5/90/0]s
QI-III	[0/22.5/−22.5/45/−45/67.5/−67.5/90]s
QI-IV	[45/−45/0/90/45/−45/0/90]s
QI-V	[0/45/−45/90/0/45/−45/90]s
QI-VI	[0/45/0/−45/90/45/90/−45]s

unidirectional composite plies with different fiber reinforcements, and to describe the applied Puck failure criterion.

3.1. Drop-weight impact test dimensioning

Following the formula for mass calculation (1), the required material density of the impactor ρ_i is determined to obtain an impactor mass m of 5.5 kg for the given volume V.

$$m = \rho_i V \tag{1}$$

The impactor is designed to have a lower height and, therefore, the overall volume. This significantly reduces the number of mesh nodes/elements for the simulation model and saves computational resources.

Table 3. Material properties of composite fibers and matrix.

Property	E-Glass Fiber [36]	T700S Fiber [37]	Kevlar 49 Fiber [38]	TDE-85 Matrix [39]
ρ (g/cm^3)	2.58	1.80	1.44	1.33
E (GPa)	72.3	230	124	4.55
G (GPa)	29.5[a]	25.0[b]	3.0[c]	1.50
υ	0.22	0.20b	0.36	0.33
σ_t (MPa)	3445	4900	3600	64.7

[a]Data from [40].
[b]Data from [41,42].
[c]Data from [43].

The rearranged formula for the kinetic energy Eq. (2) is applied to calculate the required impact velocities v corresponding to the predefined kinetic impact energies E_K.

$$E_K = \frac{1}{2} m v^2 \tag{2}$$

3.2. Rule of mixture and Hashin relation

The simple rule of mixture [29] is applied to calculate the resulting density ? of the composite materials using respective fiber and matrix densities. The required material properties for the rule of mixture and Hashin relation are listed in Table 3. Hence, the composite material density is

$$\rho = \rho_f V_f + \rho_m V_m \tag{3}$$

where ?$_f$ is fiber density; ?$_m$ is matrix density; V_f is fiber volume; V_m is matrix volume.

The rule of the mixture can also be used to calculate Young's modulus E, Poisson's ratio υ, and shear modulus G. However, it was determined that the Hashin relation is more accurate and shows a lower deviation from the experimental values than the rule of mixture [30]. Therefore, Young's modulus E_1 is calculated as.

$$E_1 = E_f V_f + E_m V_m + \frac{2(\upsilon_f - \upsilon_m)^2 V_f (1 - \upsilon_f)}{E_m (1 - \upsilon_m) L_f + \left[L_m V_m + (1 - \upsilon_m) E_f\right]} \tag{4}$$

where E_1 is longitudinal Young's modulus of the composite along fiber direction (X axis); E_f is Young's modulus of fiber; E_m is Young's modulus of matrix; υ_f is Poisson's ratio of fiber; υ_m is Poisson's ratio of matrix; L_f is fiber compliance related to Young's modulus; L_m is matrix compliance related to Young's modulus.

$$L_f = 1 + \upsilon_f - 2\upsilon_f^2 \tag{5}$$

$$L_m = 1 + \upsilon_m - 2\upsilon_m^2 \tag{6}$$

Poisson's ratio υ_{12} in XY plane is obtained as follows.

$$\upsilon_{12} = \upsilon_m - \frac{(x_m + 1) V_f (\upsilon_m - \upsilon_f)}{1 + V_m + V_f x_m + V_m (x_f - 1) \frac{G_m}{G_f}} \tag{7}$$

where G_f is shear modulus of fiber; G_m is shear modulus of matrix; x_f is fiber compliance related to Poisson's ratio; x_m is matrix compliance related to Poisson's ratio.

$$x_f = 3 - 4\upsilon_f \tag{8}$$

$$x_m = 3 - 4\upsilon_m \tag{9}$$

For unidirectional composite plies, it is assumed that Poisson's ratio in XY plane υ_{12} equals υ_{13}.

$$\upsilon_{12} = \upsilon_{13} \tag{10}$$

where υ_{13} is Poisson's ratio in XZ plane.

Following this, transverse Young's modulus of the composite (along Y-axis) E_2 can be calculated as follows.

$$E_2 = \left[\frac{\upsilon_{12}^2}{E_1} + \frac{x_m + 1}{8G_m} + \left(\frac{2 + (x_f - 1)\frac{G_m}{G_f}}{1 + V_m + V_f x_m + V_m(x_f - 1)\frac{G_m}{G_f}} - \frac{2V_f\left(1 - \frac{G_m}{G_f}\right)}{V_f + x_m + V_m\frac{G_m}{G_f}}\right)\right]^{-1} \tag{11}$$

For unidirectional composite plies, Young's modulus (along Y-axis) E_2 is equal to E_3.

$$E_2 = E_3 \tag{12}$$

where E_3 is transverse Young's modulus of the composite (along Z-axis).

Subsequently, the shear modulus in XY plane G_{12} can be determined as follows.

$$G_{12} = \frac{G_m\left(1 + V_f + V_m\frac{G_m}{G_f}\right)}{V_m + (1 + V_f)\frac{G_m}{G_f}} \tag{13}$$

Similarly to the Poisson ratio and Young's modulus, the shear modulus G_{12} of a unidirectional composite ply is equal to G_{13}.

$$G_{12} = G_{13} \tag{14}$$

where, G_{13} is shear modulus in XZ plane.

Finally, the shear modulus in YZ plane G_{23} is obtained as follows.

$$G_{23} = \frac{G_m\left(x_m + V_f + V_m\frac{G_m}{G_f}\right)}{V_m x_m + (1 + V_f x_m)\frac{G_m}{G_f}} \tag{15}$$

3.3. Puck failure criterion

The Puck failure criterion, along with maximum stress, maximum strain, Hart-Smith, Tsai-Wu, Tsai-Hill, Hashin, Chang-Chang, Hoffman, Cuntze, LaRC [31–33] and other failure criteria, are popular models for determining different failure modes in composite materials. Different CAE software might support different failure models. The puck failure criterion included in the ANSYS software package is an empirical model that takes into account the tensile, compressive, and shear stress components in a composite material. It assumes that the composite material will fail when any of these stress components exceeds a critical value determined by the ultimate material strength. The Puck failure criterion considers fiber failure (FF) and inter-fiber failure (IFF) separately [34]. Fiber failure (FF) in tensile is determined by (16), while (17) is applied for compressive fiber failure. They represent the simple maximum stress criteria.

$$\frac{\sigma_1}{X_t} = 1 \text{ if } \sigma_1 > 0 \tag{16}$$

where σ_1 is longitudinal stress (along X-axis); X_t is ultimate tensile strength in X-axis.

$$\frac{\sigma_1}{X_C} = 1 \text{ if } \sigma_1 < 0 \tag{17}$$

where X_C is ultimate compression strength in X-axis.

The same approach is valid for tensile and compressive strain.

$$\frac{\varepsilon_1}{X_{\varepsilon t}} = 1 \text{ if } \varepsilon_1 > 0 \tag{18}$$

where ε_1 is longitudinal strain (along X-axis); $X_{\varepsilon t}$ is ultimate tensile strain limit in X-axis.

$$\frac{\varepsilon_1}{X_{\varepsilon C}} = 1 \text{ if } \varepsilon_1 < 0 \tag{19}$$

where $X_{\varepsilon C}$ is ultimate compression strain limit in X-axis.

A more complex model is needed to determine IFF. For Puck's action plane strength criterion, the following seven parameters are utilized: $R_\perp^{(+)}$, $R_{\perp P}$, $R_\perp^{(-)}$, $p_{\perp P}^{(-)}$, $p_{\perp\perp}^{(+)}$, and $p_{\perp\perp}^{(-)}$. Here, the symbol R represents the fracture resistance and p is the slope parameter of the fracture curves. The symbols $\|$ and $\perp$ indicate the direction parallel to the fibers and perpendicular to them, respectively.

Mode A for matrix tension failure is identified as follows.

$$\sqrt{\left(\frac{\tau_{21}}{R_{\perp\|}}\right)^2 + \left(1 - p_{\perp\|}^{(+)}\frac{R_\perp^{(+)}}{R_{\perp\|}}\right)^2\left(\frac{\sigma_2}{R_\perp^{(+)}}\right)^2} + p_{\perp\|}^{(+)}\frac{\sigma_2}{R_{\perp\|}} = 1; \text{ if } \sigma_2 \geq 0 \tag{20}$$

where τ_{21} is shear stress along the fiber direction; σ_2 is stress normal to the fiber direction.

The occurrence of mode B for matrix compression failure is detected by applying the following formula.

$$\frac{1}{R_{\perp\|}}\left[\sqrt{\tau_{21}^2 + \left(p_{\perp\|}^{(-)}\sigma_2\right)^2} + p_{\perp\|}^{(-)}\sigma_2\right] = 1 \quad \text{if } \sigma_2 < 0 \quad \text{and} \quad 0 \leq \left|\frac{\sigma_2}{\tau_{21}}\right| \leq \frac{R_{\perp\perp}^A}{|\tau_{21C}|} \tag{21}$$

Finally, mode C for matrix shear failure is determined as

$$-\frac{R_{\perp}^{(-)}}{\sigma_2}\left[\left(\frac{\tau_{21}}{2\left(1+p_{\perp\perp}^{(-)}\right)R_{\perp\parallel}}\right)^2+\left(\frac{\sigma_2}{R_{\perp}^{(-)}}\right)^2\right]=1 \quad \text{if } \sigma_2<0 \text{ and } 0\leq\left|\frac{\tau_{21}}{\sigma_2}\right|\leq\frac{\tau_{21C}}{\left|R_{\perp\perp}^{A}\right|} \tag{22}$$

where

$$p_{\perp\perp}^{(-)}=p_{\perp\parallel}^{(-)}\frac{R_{\perp\perp}^{A}}{R_{\perp\parallel}} \tag{23}$$

$$R_{\perp\perp}^{A}=\frac{R_{\perp\parallel}}{2p_{\perp\parallel}^{(-)}}\left[\sqrt{1+2p_{\perp\parallel}^{(-)}\frac{R_{\perp}^{(-)}}{R_{\perp\parallel}}}-1\right] \tag{24}$$

$$\tau_{21C}=R_{\perp\perp}^{A}\sqrt{1+2p_{\perp\perp}^{(-)}} \tag{25}$$

The slope parameters p also referred to as Puck constants, vary depending on the composite material properties. The respective values are listed in Table 4.

$$p_{\perp\parallel}^{(+)}=p_{21+};p_{\perp\parallel}^{(-)}=p_{21-};p_{\perp\perp}^{(+)}=p_{22+};p_{\perp\perp}^{(-)}=p_{22-} \tag{26}$$

Next, the 3D stress state requires consideration to determine the occurring delamination failure, which is described as follows.

$$f_E=\sqrt{\left[\sigma_n\left(\frac{1}{R_{\perp}^{(+)}}-\frac{p_{\perp\psi}^{(+)}}{R_{\perp\psi}^{A}}\right)\right]^2+\left(\frac{\tau_{nt}}{R_{\perp\perp}^{A}}\right)^2+\left(\frac{\tau_{n1}}{R_{\perp\parallel}}\right)^2}+\sigma_n\frac{p_{\perp\psi}^{(+)}}{R_{\perp\psi}^{A}} \quad \text{if } \sigma_2\geq 0 \tag{27}$$

$$f_E=\sqrt{\left(\frac{\tau_{nt}}{R_{\perp\perp}^{A}}\right)^2+\left(\frac{\tau_{n1}}{R_{\perp\parallel}}\right)^2+\left(\sigma_n\frac{p_{\perp\parallel}^{(-)}}{R_{\perp\psi}^{A}}\right)^2}+\sigma_n\frac{p_{\perp\psi}^{(-)}}{R_{\perp\psi}^{A}} \quad \text{if } \sigma_2<0 \tag{28}$$

where f_E is stress exposure factor.

$$\sigma_n\frac{p_{\perp\psi}^{(+)}}{R_{\perp\psi}^{A}}=\frac{p_{\perp\perp}^{(+)}}{R_{\perp\perp}^{A}}\cos^2\psi+\frac{p_{\perp\parallel}^{(+)}}{R_{\perp\parallel}^{A}}\sin^2\psi \tag{29}$$

$$\cos^2\psi=1-\sin^2\psi=\frac{\tau_{nt}^2}{\tau_{nt}^2+\tau_{n1}^2} \tag{30}$$

$$R_{\perp\perp}^{A}=\frac{R_{\perp}^{(-)}}{2\left(1+p_{\perp\perp}^{(-)}\right)} \tag{31}$$

Table 4. Puck constants for GFRP [44], CFRP [44] and AFRP [45].

Constant	GFRP	CFRP	AFRP
p_{21-}	0.25	0.30	0.30
p_{22-}	0.20	0.25	0.30
p_{21+}	0.30	0.35	0.30
p_{22+}	0.20	0.25	0.30
F_{IW}	0.8	0.8	0.8
s	0.5	0.5	0.52
M	0.5	0.5	0.52

Required stresses σ_n, τ_{nt}, and τ_{n1} are determined by (32)-(34), where θ represents the angle of inclination.

$$\sigma_n=\sigma_2\cos^2\theta+\sigma_3\sin^2\theta+2\tau_{23}\sin\theta\cos\theta \tag{32}$$

$$\tau_{nt}=(\sigma_3-\sigma_2)\sin\theta\cos\theta+\tau_{23}(\cos^2\theta-\sin^2\theta) \tag{33}$$

$$\tau_{n1}=\tau_{31}\sin\theta+\tau_{21}\cos\theta \tag{34}$$

In order to determine the stress exposure factor f_E, it is imperative to conduct an iterative analysis of the angle θ to identify the global maximum, as failure will occur at this angle.

$$f_E^{(\theta)}=\begin{cases}\cos^{-1}\left(\sqrt{\frac{R_{\perp\perp}^{A}}{\sigma}}\right) & \text{if } \sigma_2<-R_{\perp\perp}^{A}\\ 0 & \text{if } \sigma_2\geq -R_{\perp\perp}^{A}\end{cases} \tag{35}$$

where

$$\frac{p_{\perp\perp}^{(-)}}{R_{\perp\perp}^{A}}=\frac{p_{\perp\parallel}^{(-)}}{R_{\perp\parallel}} \tag{36}$$

Finally, with additional consideration of a weakening factor $f_w^{(If)}$ of 0.8 to 0.9, the delamination failure can be estimated using the following formulas.

$$\frac{1}{f_w^{(If)}}\sqrt{\left[\sigma_3\left(\frac{1}{R_{\perp}^{(+)}}-\frac{p_{\perp\psi}^{(+)}}{R_{\perp\psi}^{A}}\right)\right]^2+\left(\frac{\tau_{32}}{R_{\perp\perp}^{A}}\right)^2+\left(\frac{\tau_{31}}{R_{\perp\parallel}}\right)^2}+\sigma_3\frac{p_{\perp\psi}^{(+)}}{R_{\perp\psi}^{A}}=1 \quad \text{if } \sigma_3\geq 0 \tag{37}$$

$$\frac{1}{f_w^{(If)}}\sqrt{\left(\frac{\tau_{32}}{R_{\perp\perp}^{A}}\right)^2+\left(\frac{\tau_{31}}{R_{\perp\parallel}}\right)^2+\left(\sigma_3\frac{p_{\perp\parallel}^{(-)}}{R_{\perp\psi}^{A}}\right)^2}+\sigma_3\frac{p_{\perp\psi}^{(-)}}{R_{\perp\psi}^{A}}=1 \quad \text{if } \sigma_3<0 \tag{38}$$

The active failure mode depends on both the fraction angle θ and the sign of σ_n. Inter-fiber failure modes B and C manifest exclusively in conjunction with negative σ_n. However, delamination can arise when σ_n is positive and θ equals 90°.

4. Composite material properties

4.1. Fiber and matrix

For this investigation, three different types of fibers were selected. These are AGY E-glass fiber, Toray T700S carbon fiber, and Kevlar 49 aramid fiber., TDE-307 85 with DDS curing agent epoxy resin was used as a matrix due to its advanced mechanical properties, including low shrinkage, strong adhesion, chemical stability, and high ultimate strength [35]. Figure 2 shows the respective tensile stress-strain curves.

Additionally, Table 3 presents various parameters—such as density, Young's modulus, shear modulus, Poisson's ratio, and ultimate tensile strength—which are essential for

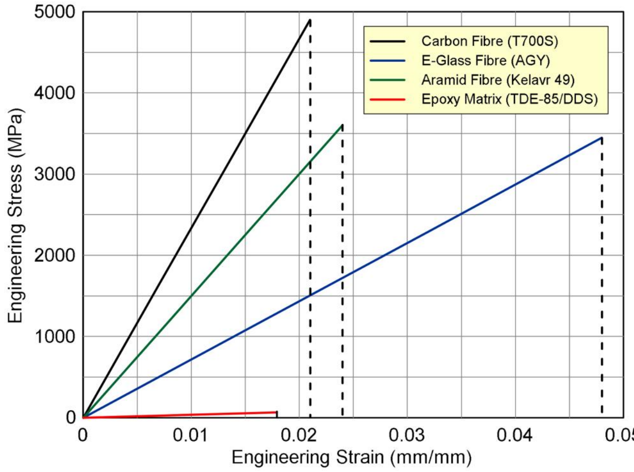

Figure 2. Tensile stress-strain curves of AGY E-glass [36], T700S carbon [37], Kevlar 49 [38] aramid fiber and TDE-85/DDS epoxy matrix [39].

Table 5. Calculated orthotropic material properties of GFRP, CFRP, and AFRP unidirectional composite plies.

Property	AGY E-Glass TDE-85/DDS	T700S TDE-85/DDS	Kevlar 49 TDE-85/DDS
ρ (g/cm^3)	2.08	1.61	1.40
V_f (%)	60	60	60
E_1 (GPa)	45.20	139.82	76.22
E_2 (GPa)	12.59	12.30	6.61
E_3 GPa	12.59	12.30	6.61
υ_{12}	0.26	0.24	0.35
υ_{23}	0.40[a]	0.38[b]	0.40[c]
υ_{13}	0.26	0.24	0.35
G_{12} (GPa)	5.05	4.91	2.25
G_{23} (GPa)	4.46	4.36	2.22
G_{13} (GPa)	5.05	4.91	2.25

[a]Not calculated, data from [44].
[b]Not calculated, data from [46].
[c]Not calculated, data from [47].

calculating the material properties of orthotropic unidirectional composite plies. All composite component materials exhibit brittle behavior as their elongation at break is below 5%.

4.2. Composite laminate

Table 5 lists the properties of the unidirectional orthotropic composite ply material for GFRP, CFRP, and AFRP calculated using the mixture rule and the Hashin relation.

In addition, the ultimate tension, compression, and shear strengths in X, Y, and Z directions were required to apply the Puck failure criterion. Although the rule of mixture can be utilized to calculate these strengths, the results obtained significantly exceed the experimental values due to the assumption of unrealistic flawlessness in the manufacturing process of the composite laminate plates. Alternatively, the ultimate strengths from several literature sources were collected and averaged, as presented in Table 6.

4.3. Puck constants

To apply the Puck failure criterion, several parameters are required, which are obtained through comprehensive testing

Table 6. Averaged ultimate strengths of GFRP, CFRP, and AFRP.

Property	AGY E-Glass TDE-85/DDS[a]	T700S TDE-85/DDS[b]	Kevlar 49 TDE-85/DDS[c]
X_t (MPa)	1104	2088	1344
Y_t (MPa)	57	34	21
Z_t (MPa)	57	34	21
X_c (MPa)	585	1131	272
Y_c (MPa)	104	162	92
Z_c (MPa)	104	162	92
S_{xy} (MPa)	75	71	42
S_{yz} (MPa)	67	60	42
S_{xz} (MPa)	75	71	42

[a]Average values calculated using ANSYS Engineering Data and [48–51].
[b]Average values calculated using ANSYS Engineering Data and [34,46, 51,52].
[c]Average values calculated using data from [45,47, 52–54].

Table 7. Material properties of steel impactor.

Property	X40CrMoV5-1 [55]
ρ (g/cm3)	1784[a]
E (GPa)	215
υ	0.28
$R_{p0.2}$ (MPa)	1190

[a]Density modified for the impactor to have a mass of 5.5 kg.

programmes [34]. The constants for GFRP, CFRP and AFRP were sourced from the literature and are listed in Table 4.

5. Impactor material properties

The drop-weight impactor is typically made of high-strength tool steel, such as X40CrMoV5-1, whose material properties are listed in Table 7. A simplified numerical implementation treating the material as exhibiting linear behavior in the elastic range is sufficient, as the impactor will not undergo any plastic deformation upon impact at low velocities and under normal testing conditions.

6. Numerical FEM setup

Simulations were executed utilizing the CAE software package ANSYS Workbench 2023 R1 Academic, employing ANSYS ACP for composite laminate modeling and Transient Structural as an implicit FEM solver. This setup is limited to a combined mesh node and element count of approximately 230k. The simulations were conducted using a PC equipped with Windows 10 64-bit operating system, 16 GB RAM, eight cores 4.20 GHz CPU and a memory size of 8GB GPU.

6.1. Utilized approach and software

For numerical investigations, the necessary material properties of impactor and support steel as well as those of GFRP, CFRP, and AFRP as test specimen material, were integrated into ANSYS Engineering Data. To create virtual models of the impactor, test specimen, and support as shown in Figure 1, each was developed in ANSYS SpaceClaim, a CAD program included in ANSYS Workbench 2023 R1. Unlike the impactor and support, the test specimen was not modeled as a solid; instead, it was created as a surface model. This is essential for

ANSYS Composite PrepPost (ACP), in which the respective composite laminate was modeled with the number of plies, ply thickness, and stacking sequence.

The finite element method (FEM) was selected for performing the simulations. FEM is widely accepted as a numerical simulation tool for designing, analyzing, and optimizing various types of structures and materials. FEM can be classified into two categories: implicit and explicit. Implicit FEM is well-suited for static and quasi-static loadings, while explicit FEM is usually employed for time-dependent scenarios where acceleration effects are significant and cannot be disregarded. Therefore, explicit FEM is the ideal tool for dynamic loadings, where the total forces are equal to the mass multiplied by acceleration [56]. Regrettably, the ANSYS explicit FEM solver Explicit Dynamics, included in ANSYS Workbench 2023 R1, exhibits partial compatibility with ANSYS ACP, as it cannot import layered elements relevant for evaluating composite laminate plates and individual plies. As a result, the integration of composite failure criteria is not possible. Such issues do not arise with ANSYS Transient Structural; however, this application adopts an implicit FEM approach. Despite this, the use of ANSYS Transient Structural remains feasible, as the solver breaks down the dynamic problem into a series of steady-state implicit problems, which are then combined to create a displacement over time. It is important to note that this approach is only suitable for low velocities.

A key factor contributing factor to the explicit/implicit difference is that explicit solvers inherently incorporate automatic body self-contact calculation, a feature not found in implicit solvers. Therefore, the contact types must be created manually, leading to increased complexity in the simulation setup and potential challenges in achieving convergence. Furthermore, another difference lies in the behavior of the explicit solver, which promptly eliminates failed elements during the solution process, allowing the solver to proceed reliably and display material destruction. In contrast, the implicit solver requires significantly more preparatory work to remove failed elements and can result in convergence issues during operation. After considering and evaluating these factors, it was decided that ANSYS Transient Structural is suitable for low-velocity drop-weight impact testing and thus it was employed for the simulations in this research project.

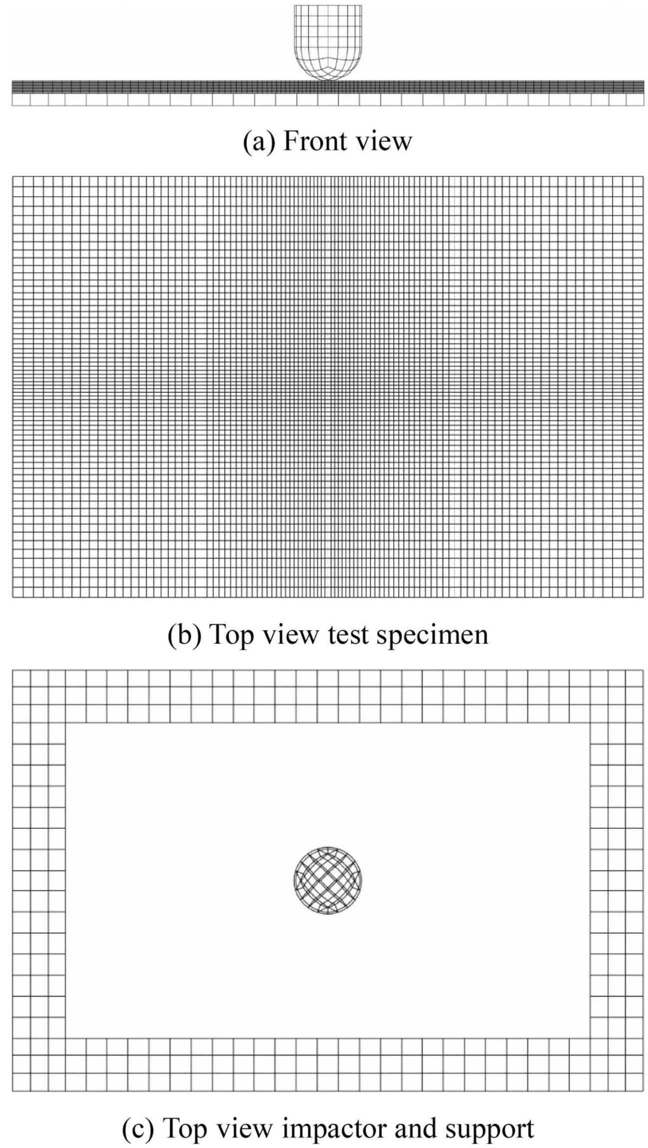

Figure 3. Generated mesh of drop-weight impact test setup.

6.2. Mesh generation

The simulation setup featured only Lagrangian meshes. The impactor mesh, shown in Figure 3(a), was automatically generated with an element size of 2.5 mm and activated capture curvature. For the test specimen mesh illustrated in Figure 3(b), a face meshing method using quadrilateral elements was applied, with a body sizing of 2 mm and an edge sizing of 1.5 mm for all four edges, incorporating a factor of three bias toward the center. This results in a progressively finer mesh toward the impact zone, allowing for more accurate results. Regarding the mesh of the support shown in Figure 3(c), a face meshing method using quadrilateral elements and a body sizing of 5 mm was employed. The coarser meshes are justified by the fact that the steel components of a drop-weight impact test do not undergo major deformation and only the impact behavior of the test specimen was of primary interest. The complete drop-weight impact test mesh comprised 120,036 nodes and 107,626 elements. ANSYS provides guidelines for quality thresholds to achieve excellent meshes. According to ANSYS recommendations, certain indicators, such as minimum element quality, should be maintained above 0.2 [57], and the skewness ratio should not exceed 0.95. Ideally, an aspect ratio should be less than 10 [58]. In the case of the generated drop-weight impact test setup mesh, a minimum element quality of 0.11, a maximum skewness of 0.84 and an aspect ratio of 13.41 were measured. Although the element quality and aspect ratio failed to achieve their respective thresholds, the mesh was still deemed satisfactory. Most of the mesh elements were simple geometries and the poorer quality values were attributed to the low ply thickness of the composite laminate in relation to length and width.

6.3. Simulation boundary conditions

In configuring the ANSYS Transient Structural module, no-separation contact behavior was defined in the contact region between the impactor and the test specimen. Although this type of contact did not permit the two bodies to separate, it did allow them to slip, which became increasingly important as the angle of impact increased. A bonded contact was defined between the contact surface of the test specimen and the support, preventing any separation movement. The impactor was assigned a velocity in the Y direction and was constrained from moving in the X or Z directions by applying a remote displacement. This measure ensured that the impactor did not deflect during an oblique impact. Additionally, both the impactor and the test specimen were subjected to standard gravity, while the bottom surface of the support was fixed. The described boundary conditions are illustrated in Figure 4. In the analysis settings, a simulation duration of 6–8 ms was defined, depending on the time required for the test specimen to return to its initial position after impact. Substeps, during which the implicit FEM solver calculated a result, occurred every 0.1 ms.

Regarding the desired types of solutions, the history of the impactor's kinetic energy and the histories of the transmitted Y and X-components of the contact forces were recorded. For the test specimen, a history of total deformation and von Mises stress was obtained, with stress distribution contours determined for each individual ply. Finally, the Puck Inverse Reverse Factor (IRF) was calculated to indicate the damage severity of the test specimens and to investigate the delamination areas of the individual plies. A delamination weighting factor of 1.69 was defined for both 10 J and 15 J impact energy related simulations to ensure that the delamination area results were accurate and consistent with the experimental results of the validation case.

6.4. Validation case

The numerical validation case is based on the experimental results of Falco et al. [27]. It was developed using the same geometries and dimensions as the drop-weight impact test setup following ASTM D7136/D7136M standard [28]. The overall thickness, number of plies, and ply thickness of the composite laminate plates were also identical. Furthermore, the mesh configuration and the simulation boundary conditions remained the same. The only differences were that Falco et al. [27] used a different HexPly AS4/8552 CFRP and a different stacking sequence, which were applied in the numerical validation case. These were the only parameters, alongside the impact angle, that changed in the main simulations of this research project. Additionally, while the impact velocities were slightly different, the impact energies were identical. Moreover, the rubber pins were omitted for simplicity.

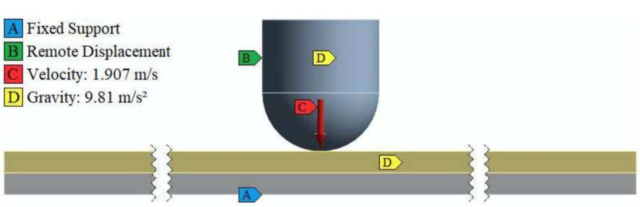

Figure 4. Boundary conditions of 10 J drop-weight impact test setup.

7. Results and discussion

The quality of the numerical FEM results was subjected to certain limitations. First, an unrestricted number of elements and nodes could have improved the accuracy of the results. Second, the results were calculated every 0.1 ms; however, the events occurring between these timestamps were not captured. Third, by omitting the rubber pins that hold the test specimen in place and instead implementing a bonded contact type between the test specimen and the support, the surfaces in contact with the support behaved differently, leading to altered stress distributions near the transition from the test specimen to the support cutout. However, the impact zone remained unaffected. Lastly, only the delamination caused by 0° impacts was validated, while the delamination areas resulting from oblique impacts may be subject to deviations.

7.1. Results of validation case

The results obtained from the validation case demonstrated a strong correlation between the proposed numerical and experimental results. Table 8 shows that the deviation between the results is less than 1%. The extent of the delamination area was measured at the maximum von Mises stress, as this represents the combined effect of normal and shear stresses, which are key factors in the initiation and growth of delamination. When stress values reach critical levels, particularly in impact zones, they can induce interlaminar shear stresses that lead to delamination. Delamination is the most relevant type of interlayer damage under low-velocity impact. Other types of interlayer damage such as fiber and matrix cracks as well as fiber breakage are the types of damage that occur more frequently under high-velocity impacts.

Despite some expected differences in material performance under the impact that occurred between simulation and experiment, the representation of the delamination damage as a uniform contour (Figure 5) is fully appropriate. Figure 5 shows that the numerical delamination areas are much more circular and nearly symmetrical in both the X and Z directions. In contrast, the experimental delamination areas became increasingly elongated with higher impact energy. This geometrically different behavior can be attributed to the assumption of a flawlessly manufactured composite laminate plate in the numerical model, where all cohesion and adhesion were uniform. In reality, both the

Table 8. Correlation of delamination area in the validation case.

Impact Energy	Experimental [28]	Numerical	Deviation
10 J	379.2 mm^2	377.9 mm^2	0.34%
15 J	663.4 mm^2	662.3 mm^2	0.17%
18 J	883.4 mm^2	876.0 mm^2	0.84%

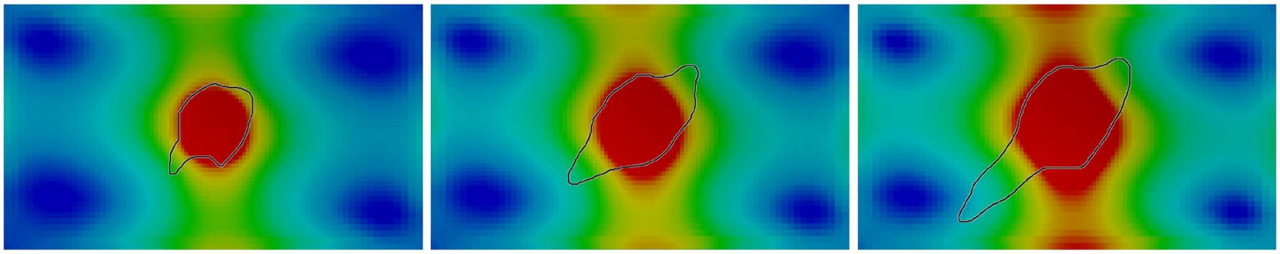

(a) Impact energy 10 J (b) Impact energy 15 J (c) Impact energy 18 J

Figure 5. Validation case 125 × 75 mm cutouts of the numerical delamination contours with experimental outlines as a comparison.

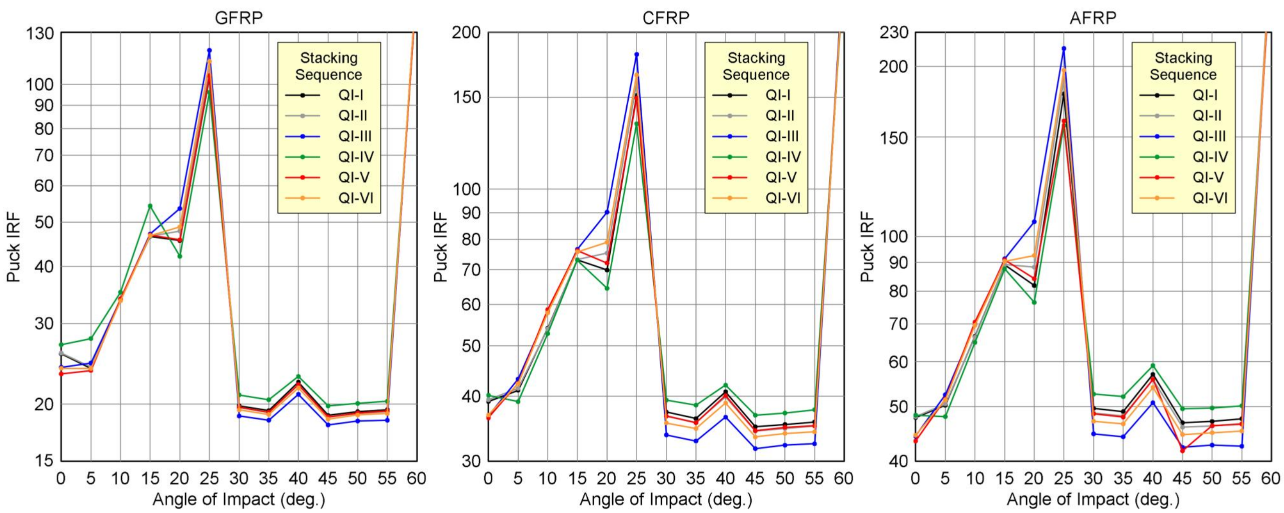

(a) GFRP (b) CFRP (c) AFRP

Figure 6. Influence of stacking sequences on the puck IRF of composite laminate plates subjected to a 10 J oblique impact ranging from 0° to 60°.

materials and the manufacturing process are subject to certain tolerances, which influence the impact outcome. The numerical delamination near the outer edges of the cutout is negligible, as it was caused by the bonded contact type between the test specimen and the support. Due to the increasing deviation between the numerical and experimental delamination with higher impact energy, it was decided to conduct the following simulations primarily at 10 J and partially at 15 J. The configuration with 18 J impact energy was not further investigated.

7.2. Stacking sequence

The effects of different stacking sequences on the Puck IRF of composite laminate plates subjected to oblique impacts ranging from 0° to 60° are shown in Figure 6. The Puck IRF considers fiber failure, matrix tension, matrix compression, and matrix shear failure and delamination. A higher value indicates greater damage, while a value below 1 suggests that the composite laminate plate remains undamaged.

GFRP, CFRP and AFRP were all investigated, whereby GFRP exhibited the lowest Puck IRF, followed by CFRP and then AFRP. Although the mechanical properties of aramid are capable of absorbing the energy of high-velocity impacts, it has a relatively weak ultimate compressive strength compared to other materials. While CFRP generally demonstrates higher ultimate strength, it is also significantly stiffer due to its high Young's modulus. Thus, the impact energy is not easily distributed throughout the material; instead, it tends to concentrate in the impact zone, where higher stresses lead to greater damage. The Puck IRF histories of the different stacking sequences were similar.

The level of damage increased rapidly as the impact angle of impact rose to 25°. However, most stacking sequences (with the exception of QI-III and QI-IV) momentarily displayed a declining gradient or a slight decrease at an impact angle of 20°. For the stacking sequence QI-III, the Puck IRF increased more steeply, while for QI-IV it decreased more rapidly. As the impact angle approached 30°, the Puck IRF for all stacking sequences dropped sharply and remained relatively constant up to an impact angle of 55°, although a slight increase was observed at 40°. At higher impact angles, the impactor caused significant damage to the upper plies of the composite laminate. The rapid increase in the Puck IRF up to an impact angle of 25°, followed by a subsequent decrease, was similarly noted by Rawat et al. [25], who attributed this phenomenon to the generation of random subsurfaces between plies. For GFRP, CFRP, and AFRP, most stacking sequences behaved similarly, except for QI-IV in GFRP, which exhibited a more pronounced rise in Puck IRF

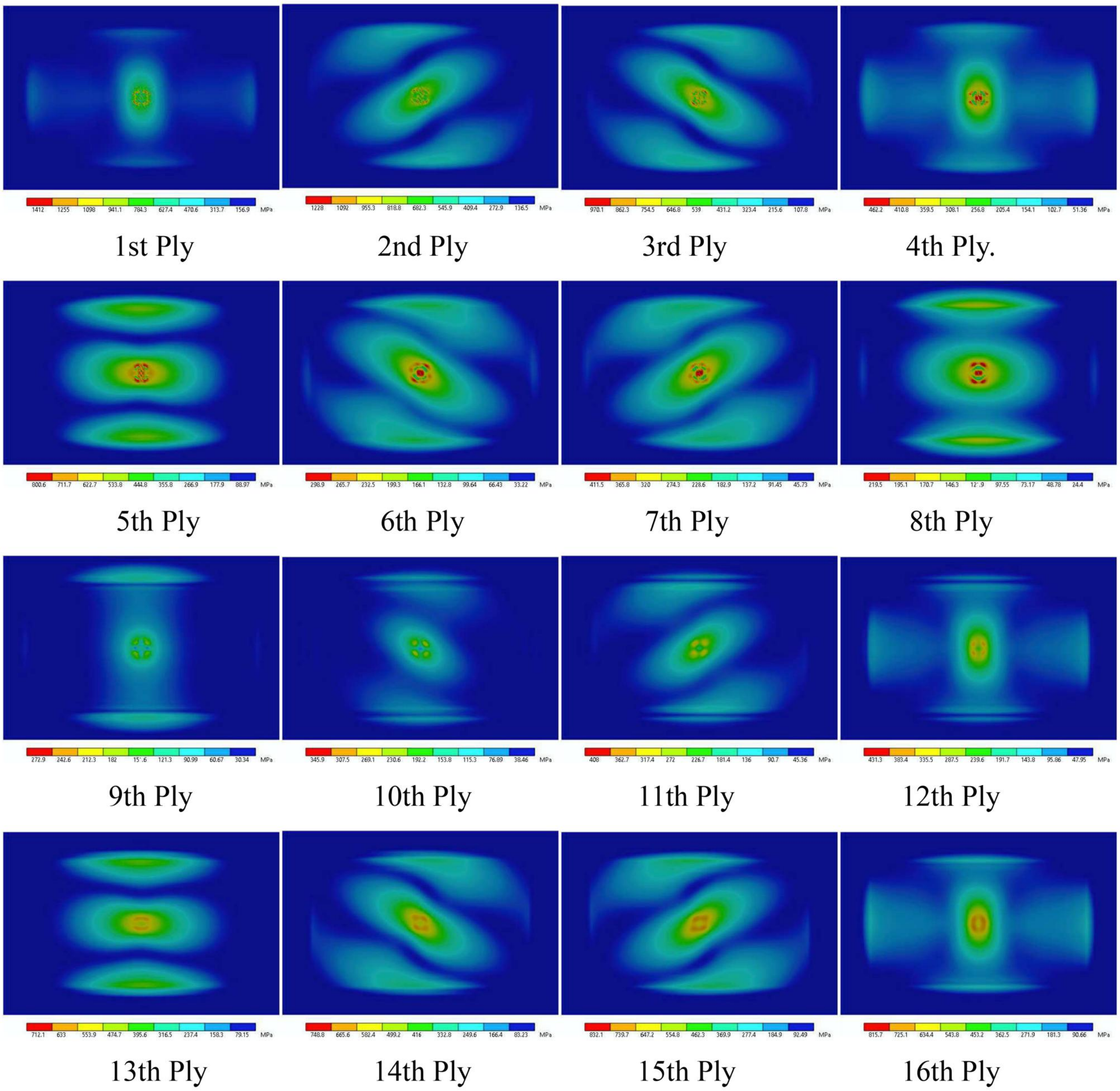

Figure 7. Top view von mises stress contours of GFRP plies with stacking sequence QI-V under 10 J impact at the angle of 0°.

compared to the other stacking sequences up to an impact angle of 15°.

In comparison to CFRP and AFRP, the deviations between the individual stacking sequences for GFRP were less pronounced. An exception occurred for AFRP with stacking sequence QI-V at an impact angle of 45°, where the Puck IRF momentarily dipped. When assessing the best performing stacking sequence for CFRP and AFRP, the stacking sequence QI-IV was superior for oblique impacts ranging from 0° to 25°, while the stacking sequence QI-III was the least efficient. However, from an impact angle of 30° onwards, this trend is reversed where the stacking sequence QI-III becomes the highest performing. This can be explained by the fact that at steeper impact angles, stacking sequences featuring a 0° first ply orientation with the following plies having only a slightly wider ply orientation angle, perform better; in this case, the angle was ±22.5°.

Overall, the highest performance across the entire range of oblique impacts was achieved by the stacking sequence QI-V for GFRP, by the stacking sequences QI-I, QI-IV, and QI-V for CFRP, and by the stacking sequences QI-IV and QI-V for AFRP. The stacking sequences QI-II, and QI-VI performed poorly overall and are not recommended. In summary, the stacking sequence QI-V is a satisfactory compromise for GFRP, CFRP, and AFRP across the entire range of impact angles. Therefore, the following simulations all utilized the QI-V stacking sequence.

7.3. Von Mises stress

The von Mises stress contours for the GFRP plies with stacking sequence QI-V under 10 J and 0° impact are presented in Figure 7, providing a top view of each of the 16 individual plies. The von Mises stress patterns are different for each individual ply and depend on the respective ply orientation. Specifically, the 1st, 6th, 9th, and 13th plies have a 0° orientation while the 4th, 8th, 12th, and 16th plies are oriented at 90°. The remaining plies are oriented at either +45° or −45°. The 1st ply, directly exposed to the impactor, exhibited a concentration of von Mises stress in the immediate vicinity of the impact zone.

The von Mises stress gradually spread over a broader area across the subsequent three plies. In the 5th to 8th plies, the stress was more evenly distributed, and the direct load from the impactor began to dissipate slightly. From the 9th ply onwards, the von Mises stress appeared to decrease; however, this was due to the primary stress shifting to the underside of the plies in the latter half of the composite laminate plate. For the bottom four plies, the von Mises stress distribution intensified further, as these plies are positioned farther from the neutral axis and were therefore subject to greater bending, leading to increased tension.

In addition, the contact between the test specimen and the support induced some stress. When examining the von Mises stress magnitudes, the highest levels were observed directly in the impact zone and adjacent plies, decreasing through the middle plies and then increasing from the 13th ply onwards. However, the peak von Mises stress in the impact zone was not matched elsewhere, and the stress in the bottom plies was distributed over a considerably wider area. In general, the plies with 90° orientation experienced lower von Mises stress. However, these plies are important for achieving quasi-isotropic behavior and could play a more significant role under different impact conditions. Since the outer plies of the composite laminate plate were subjected to the highest von Mises stress, while the middle plies near the neutral axis experienced significantly lower stress, it would be reasonable to replace only the outer plies with a higher-performing composite material. This approach would create a hybrid composite laminate plate, rather than manufacturing the entire composite laminate plate from the superior composite material, which would incur significantly higher costs.

7.4. Kinetic energy and contact force

The kinetic energy history of the impactor at 10 J and 15 J oblique impact on GFRP, CFRP, and AFRP composite laminate plates is shown in Figure 8.

In general, the kinetic energy decreased in a mainly linear fashion, with only a minor change at the onset of impact and a flattening of the curve toward the end of the impact. The shortest impact duration, and thus the steepest decline in kinetic energy, occurred during the impact on the CFRP laminate plate in Figure 8(b), owing to its high stiffness. In contrast, the impact durations of the GFRP and AFRP laminate plates in Figure 8(a,c) were significantly longer, with AFRP showing only a slightly increased impact duration. Furthermore, 60° impacts demonstrated the shortest impact duration, followed by 0° and concluded with 30° impacts. The variation in impact duration across 0°, 30°, and 60° impacts was least pronounced for CFRP and most pronounced for GFRP. The time intervals were relatively similar for GFRP, whereas for CFRP and AFRP the difference between the impact durations of 60° and 0° impacts was significantly smaller than the between 0° and 30° impacts.

Regarding the impact contact forces between the impactor and test specimen, Figure 9 displays them separated into Y- and X-components for GFRP, CFRP, and AFRP at 10 J and 15 J with impact angles of 0°, 30°, and 60°. The Y-component aligns axially with the impactor's direction, while the X-component is radial to it. In general, 30° impacts demonstrated the lowest Y-component contact force, followed by the 0° impacts, with the highest force observed for the 60° impacts. In contrast, the X-component contact force was highest for the 30° impacts, significantly lower for the 60° impacts and almost non-existent for the 0° impacts, as expected. Considering the different materials impacted, the CFRP laminate plate in Figure 9(b) experienced the highest Y-component contact forces, likely due to its high stiffness and limited stress distribution capability. As for the X-component of the contact force, CFRP exhibited the highest contact force at 30° impacts compared to

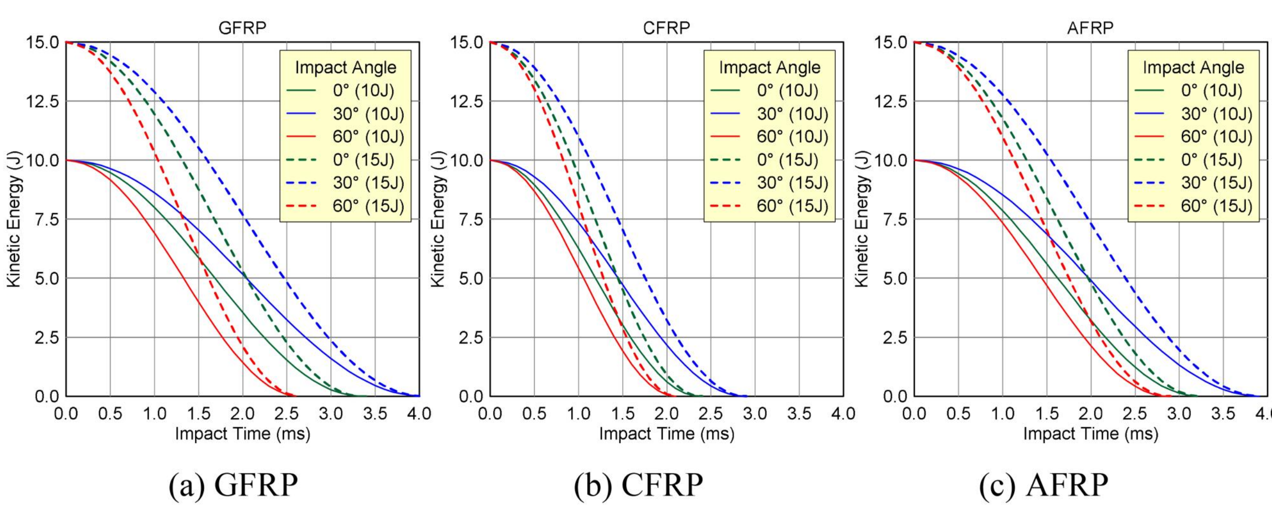

Figure 8. Kinetic energy history of the impactor during 10 J and 15 J oblique impacts on composite laminate plates with stacking sequence QI-V.

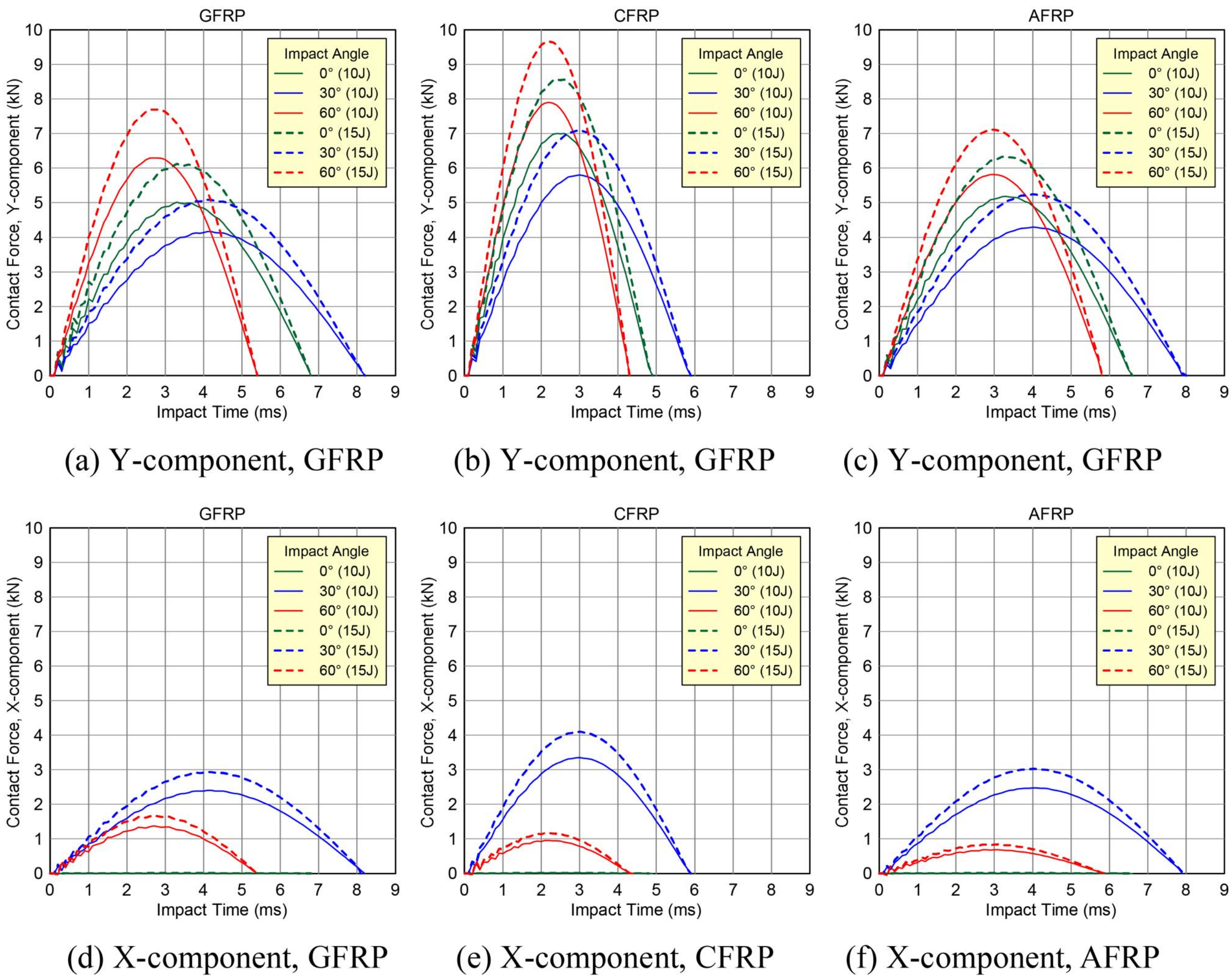

Figure 9. Contact force history caused by the impactor during 10 J and 15 J oblique impacts on composite laminate plates with stacking sequence QI-V.

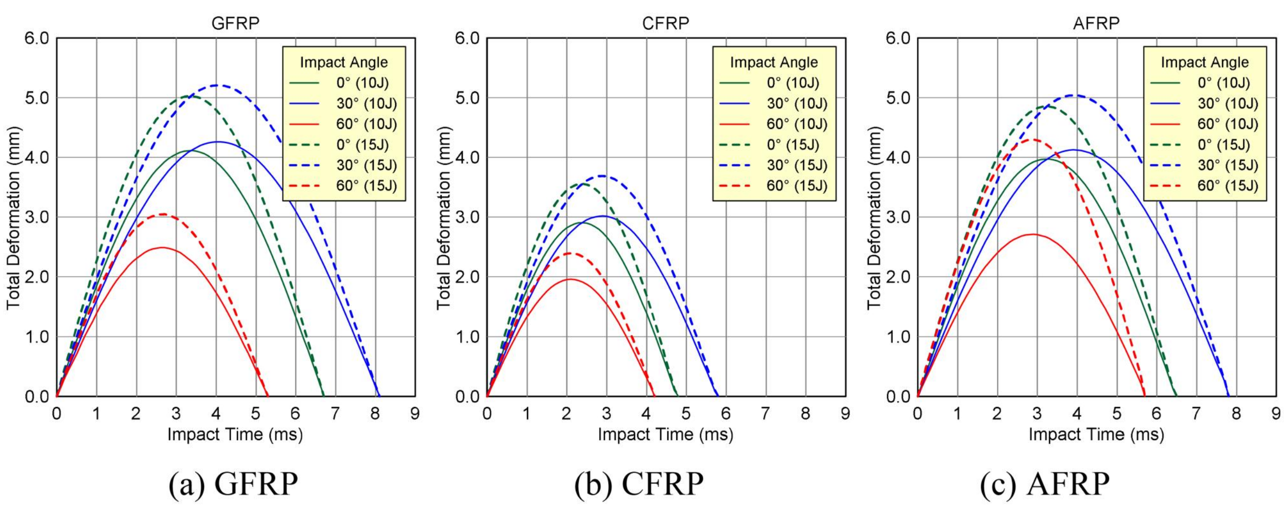

Figure 10. Total deformation history of composite laminate plates with stacking sequence QI-V under 10 J and 15 J oblique impacts.

GFRP and AFRP, but relatively low forces at 60° impacts. In comparison, the GFRP and AFRP laminate plates in Figure 9(a,c) were subject to lower contact forces. For GFRP, the Y-component of the contact force was higher than for AFRP at 60° impacts, yet lower at 0° and 30° impacts. As for the X-component of the contact force, it was similar for both GFRP and AFRP at 0° and 30° impacts, but different at 60°, where GFRP exhibited the highest contact force of all investigated composite materials, while AFRP was exposed to the lowest.

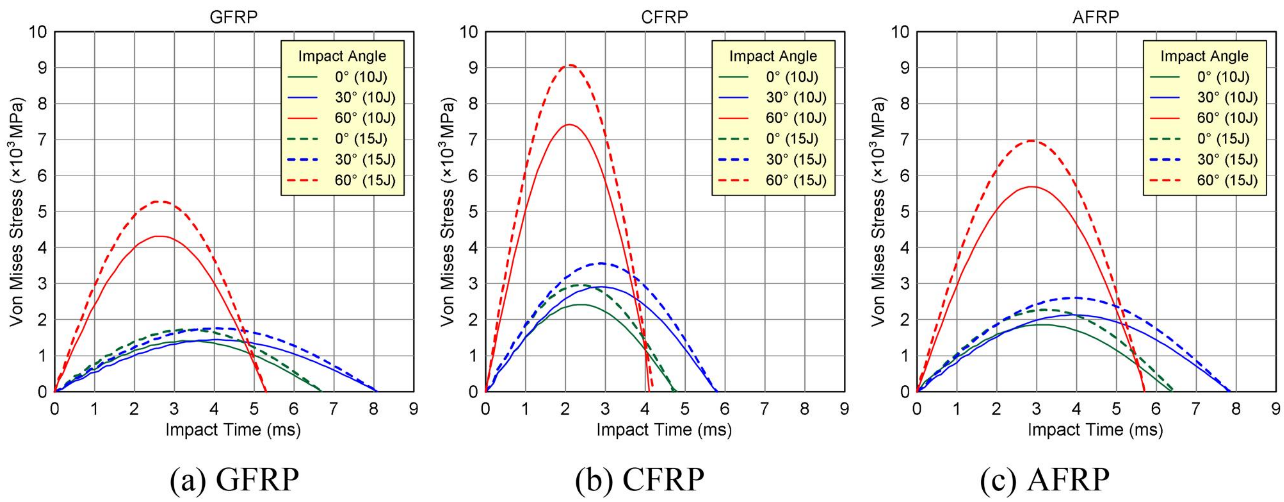

Figure 11. Von mises stress history of composite laminate plates with stacking sequence QI-V under 10 J and 15 J oblique impacts.

7.5. Total deformation

The total deformation history of the GFRP, CFRP, and AFRP laminate plates under 10 J and 15 J impacts at angles of 0°, 30°, and 60° is presented in Figure 10. As a general tendency, 60° impacts caused the lowest total deformation, while impacts at 0° and 30° led to considerably higher total deformation, with the latter being slightly more intense. As expected, the CFRP composite laminate plate in Figure 10(b) experienced the least total deformation due to its superior stiffness. Regarding the GFRP and AFRP laminate plates in Figure 10(a,b), they demonstrated similar behavior, with GFRP showing higher total deformation than AFRP at 0° and 30° impacts, but the trend reversed at 60°. Additionally, at a 15 J and 60° impact on AFRP, the total deformation was increased disproportionally compared to its 10 J impact counterpart; this response was not observed for GFRP and CFRP.

The von Mises stress history of the GFRP, CFRP, and AFRP laminate plates associated with the previous total delamination history is shown in Figure 11. For 0° and 30° impacts, a general trend was observed: higher von Mises stress resulted in greater total deformation. However, for 60° impacts, the von Mises stress—likely concentrated in the upper plies and limited in distribution due to the steep impact angle—was the highest, while total deformation was the lowest. With respect to the material, it is unsurprising that the CFRP laminate plate in Figure 11(b) exhibited the highest von Mises stress, attributed to its high stiffness and consequently reduced ability to distribute stresses. Interestingly, while the total deformation of the GFRP and AFRP laminate plates in Figure 11(a,c) was similar, the difference in von Mises stress magnitude was significant. AFRP experienced much higher von Mises stress, which is logical, as this level of stress is needed to achieve a similar total deformation to GFRP despite AFRP's greater stiffness.

7.6. Delamination

The delamination contours of the 1st, 8th, and 16th plies for GFRP, CFRP, and AFRP resulting from 10 J impact at the angle of 0° are shown in Figure 12. For the 1st ply with 0° orientation, GFRP in Figure 12(a) exhibited the largest delamination area compared to CFRP and AFRP in Figure 12(d,g). The shape and size of the delamination for CFRP and AFRP were similar; however, AFRP showed a greater tendency for delamination expansion, as indicated by the yellow outline surrounding the red delamination area. This is because AFRP distributed the impact forces further from the impact zone. For the 8th ply with 90° orientation, GFRP in Figure 12(b) had the smallest delamination area, which was more elongated than circular, unlike CFRP in Figure 12(e) and AFRP in Figure 12(h). The delamination observed along the edges was due to the bonded contact type between the test specimen and the support and would not have occurred in an unsimplified drop-weight impact test. The delamination areas of the 16th ply with 0° orientation varied more significantly. The most distinct delamination occurred for GFRP in Figure 12(c), while almost none was observed for CFRP in Figure 12(f). The AFRP in Figure 12(i) showed a similar pattern to CFRP but was more pronounced.

The delamination contours for the 1st, 8th, and 16th plies of the GFRP, CFRP, and AFRP laminate plates under 10 J impact at the angle of 30° are illustrated in Figure 13. Unlike the delamination areas caused by 0° impacts, these areas are considerably smaller for the 1st ply with 0° orientation, while the delamination area of GFRP in Figure 13(a) becoming more elongated. The delamination area of CFRP in Figure 13(d) was smaller than that of AFRP in Figure 13(g) and neither was elongated in contrast to that of GFRP. For the 8th ply with 90° orientation, the delamination areas remained almost identical across all materials as shown in Figure 13(b,e,h). Similarly to the 1st ply, the delamination area of GFRP in Figure 13(c) became smaller and more elongated compared to the area caused by the 0° impact. In contrast, the delamination areas of CFRP and AFRP in Figure 13(f,i) increased.

Finally, Figure 14 presents the delamination contours caused by 10 J impact at the angle of 60°. In contrast to the delamination areas seen in 0° and 30° impacts, the differences between the materials became more uniform. For the 1st

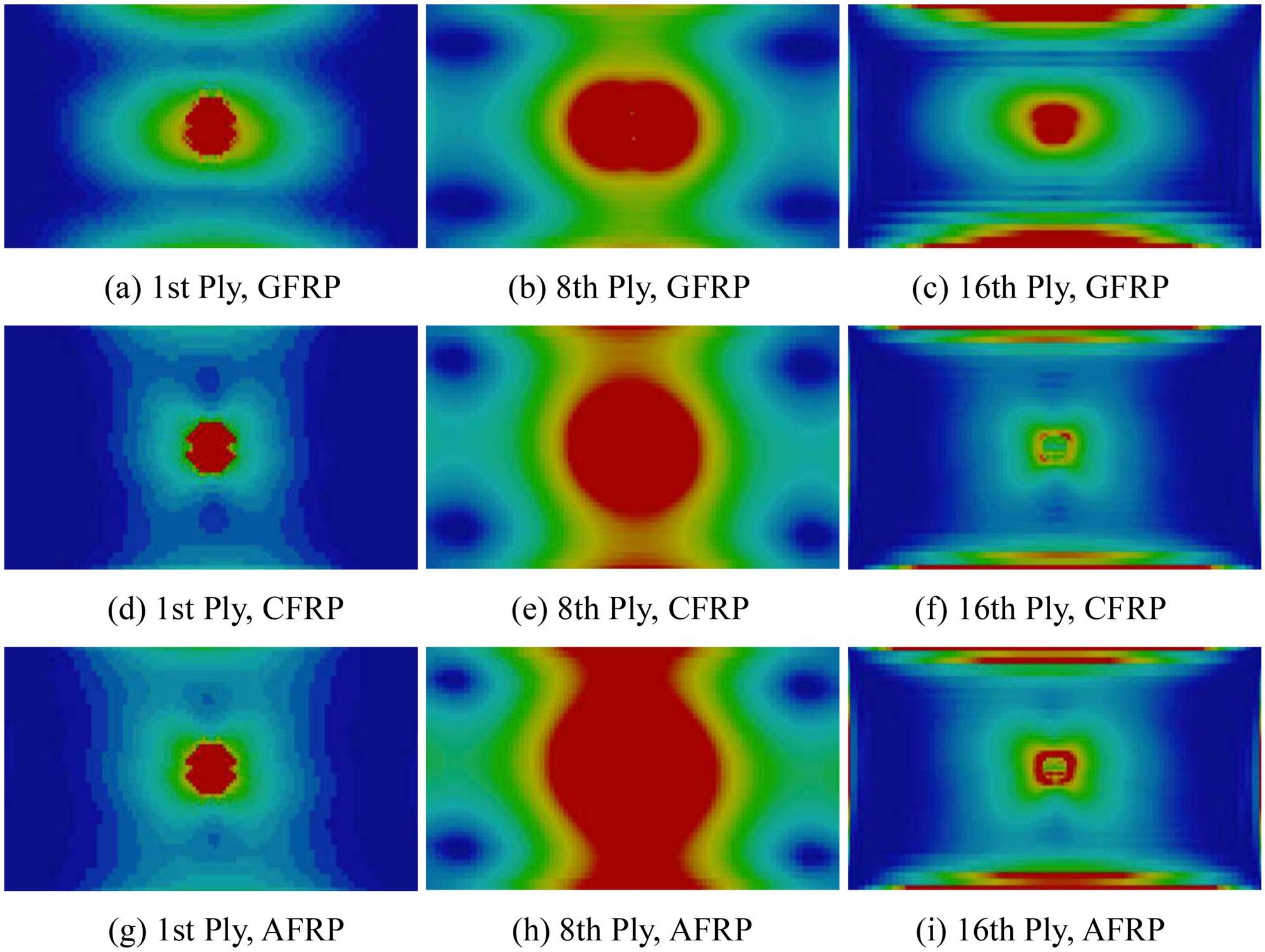

Figure 12. Top view of 125×75 mm cutout delamination contours of GFRP, CFRP, and AFRP plies with stacking sequence QI-V under 10 J impact at the angle of 0°.

ply with 0° orientation, GFRP, CFRP, and AFRP in Figure 14(a,d,g) exhibited similar delamination shapes and sizes. However, the entire CFRP and AFRP laminate plate was subjected to a certain amount of stress. The delamination areas of the 8th ply with 90° orientation also displayed changes. The altered shape of GFRP is shown in Figure 14(b), while the delamination areas for CFRP in Figure 14(e) and especially AFRP in Figure 14(h) decreased significantly. Regarding the 16th ply with 0° orientation, the delamination areas of all materials were similar in shape to those of the 1st ply, with CFRP being slightly smaller.

In general, the largest delamination areas of the outer plies were observed in GFRP, whereas the smallest areas were found in CFRP. The size of the delamination area is presumably related to the material's ability to distribute the stresses caused by the impact over a larger area. However, this larger delamination area features a lower Puck IRF, indicating that the threshold at which damage occurs is higher; consequently, the composite laminate plate may remain fully intact at lower impact energies. In contrast, CFRP exhibited a smaller delamination area, as the stresses from the impact tend to remain localized and demonstrate higher concentration, which justifies the occurring higher Puck IRF. Due to the weaker stress distribution, the damage threshold of the CFRP laminate plate is significantly lower. The inferior performance of the AFRP 8th ply at low-velocity impact can be attributed to its higher stiffness compared to GFRP, as well as its significantly lower ultimate strength. However, AFRP possesses a substantially lower density than GFRP. The delamination shape and size are also dependent on the ply orientation. For instance, a ply orientation of 0° typically results in the lowest delamination, while a 90° ply orientation leads to the largest delamination area, with the $\pm 45^\circ$ plies located in between. Regarding potential differences at 15 J impact, the delamination areas only increased slightly compared to their respective 10 J impact counterparts, whereas the delamination shape remained the same.

8. Conclusions

This study provides a numerical analysis of the performance of composite laminates and the damage occurring under low-velocity oblique impact, which is the most common hazard for materials across a large variety of industrial applications. Three types of composite materials (GFRP, CFRP, and AFRP), each with different stacking sequences, were investigated using ANSYS simulation to analyze the behavior during the impact event. The main findings derived from this study are summarized as follows.

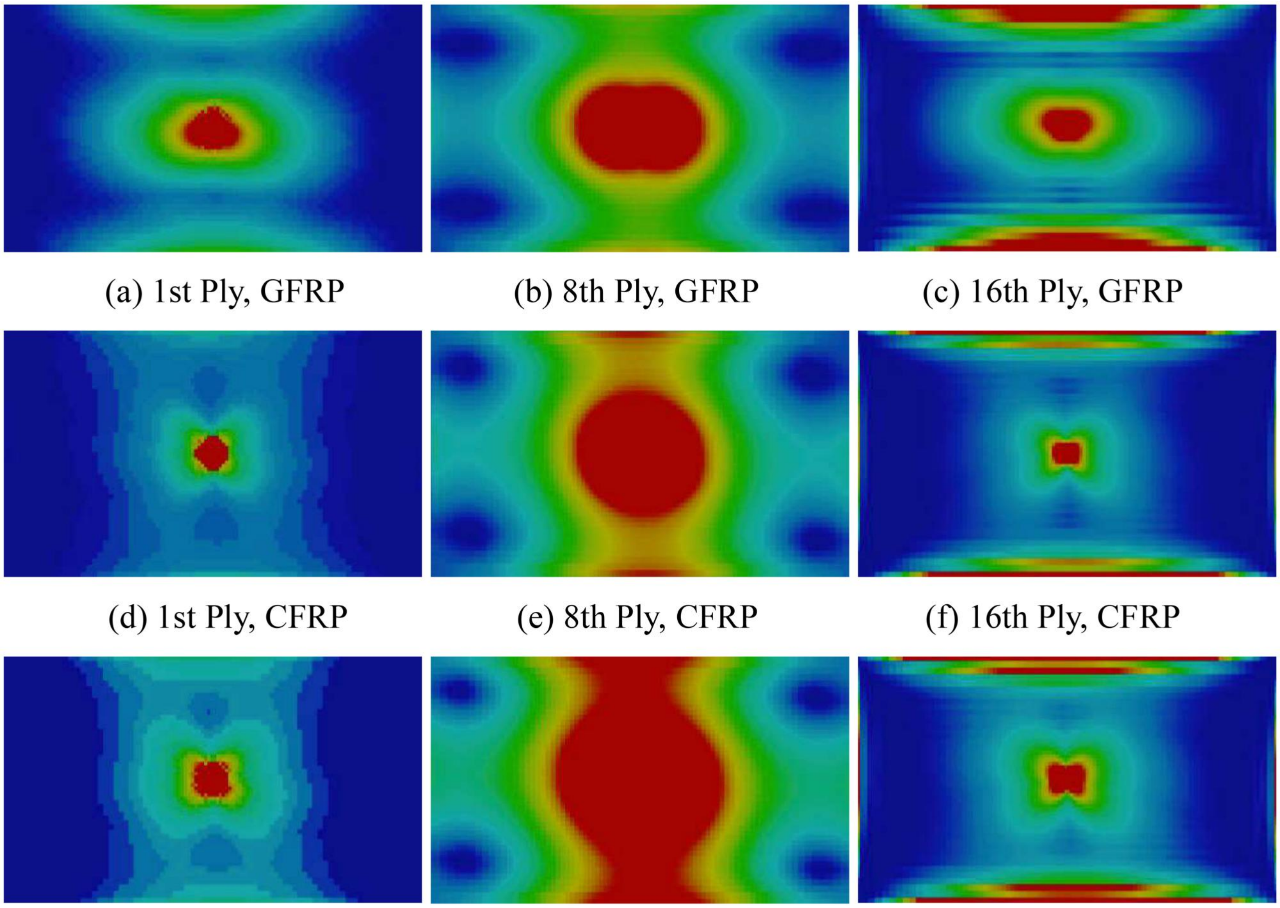

(a) 1st Ply, GFRP (b) 8th Ply, GFRP (c) 16th Ply, GFRP

(d) 1st Ply, CFRP (e) 8th Ply, CFRP (f) 16th Ply, CFRP

(g) 1st Ply, AFRP (h) 8th Ply, AFRP (i) 16th Ply, AFRP

Figure 13. Top view of 125 × 75 mm cutout delamination contours of GFRP, CFRP, and AFRP plies with stacking sequence QI-V under 10 J impact at the angle of 30°.

- Damage to composite laminate plates caused by low-velocity impact increases significantly up to an impact angle of 25°. Beyond the angle of 25°, the level of damage decreases rapidly and remains relatively constant up to an impact angle of 55°. Subsequent impact angles cause extensive damage.
- To minimize Puck IRF, the stacking sequence QI-V [0/45/−45/90/0/45/−45/90]s is the best compromise for GFRP, CFRP, and AFRP considering the entire range of impact angles. However, specifically for impact angles ranging from 0° to 25°, QI-IV [45/−45/0/90/45/−45/0/90]s is optimal for CFRP and AFRP (excluding GFRP). From an impact angle of 30° onwards, the most appropriate stacking sequence is QI-III
- [0/22.5/−22.5/45/−45/67.5/−67.5/90]s.
- The highest von Mises stresses, which are more likely to cause damage, occur directly in the impact zone on the upper plies of the composite laminate plate. The next highest von Mises stresses are found in the lower plies, which are subjected to tension due to impact-induced deflection. The lowest von Mises stresses are observed for the plies located in the middle of the composite laminate plate near the neutral axis. Therefore, it would be reasonable to replace only the outer plies with composite material exhibiting better performance characteristics, thereby creating a hybrid composite laminate plate. Such an approach is an alternative to manufacturing the entire composite laminate plate using the higher-performing material, which would result in significantly higher costs.
- The observed trend reveals that the impacted composite laminate plates with a lower deflection response due to higher stiffness are affected by higher von Mises stresses, as they can not propagate as far from the impact zone. When the individual ultimate strengths of different composite materials are disregarded, this usually results in a smaller delamination area, but the damage initiation threshold is lower. Conversely, a larger von Mises stress distribution leads to a larger delamination area, but the delamination occurs at higher impact energies. Among the composite materials used for this investigation, GFRP plies with 0° orientation show larger delamination areas than those of CFRP and AFRP; however, in plies with 90° orientation delamination areas are significantly less pronounced.

For future research, incorporating four rubber pins into the numerical drop-weight impact test setup, which exerts

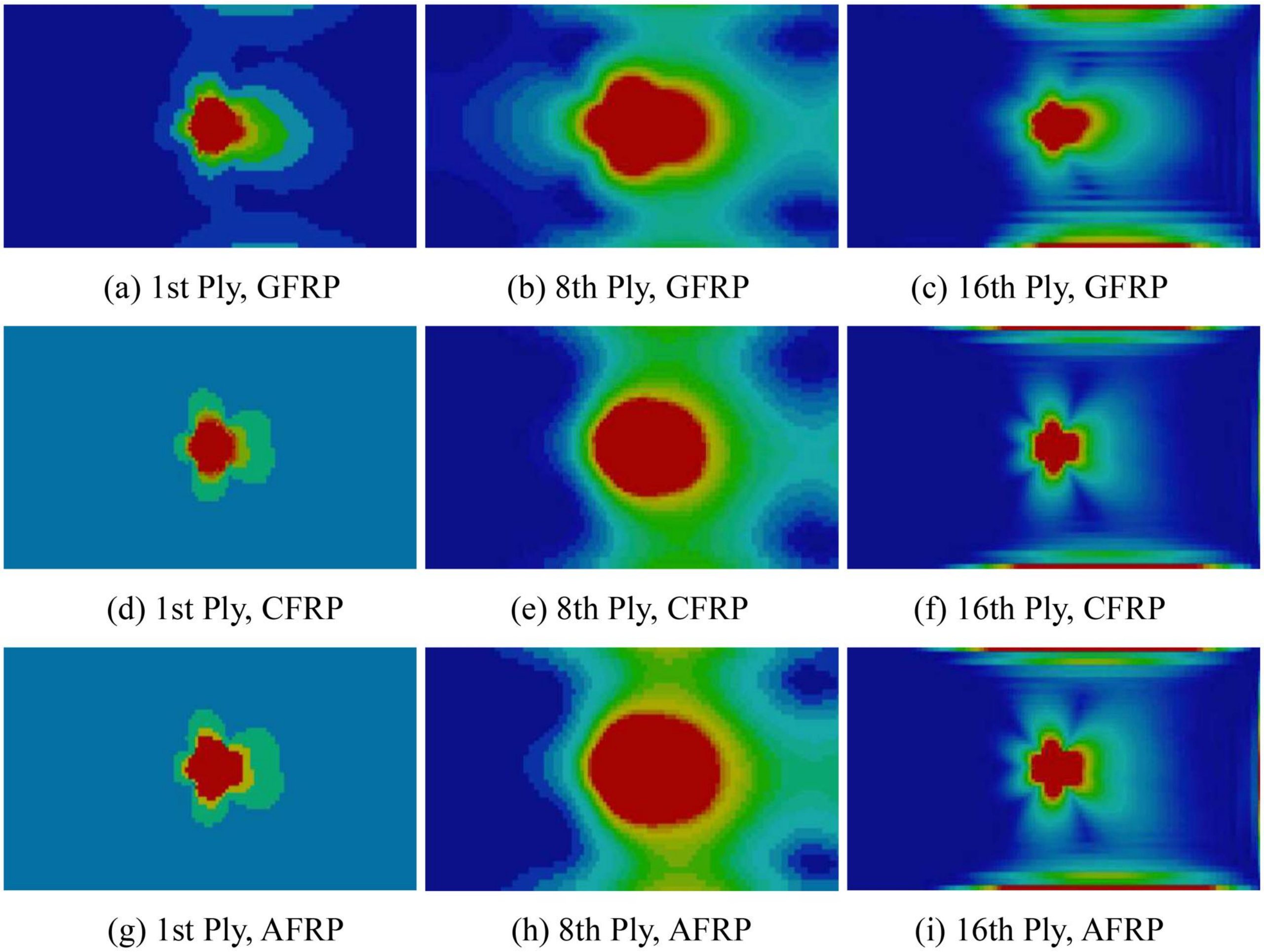

Figure 14. Top view of 125×75 mm cutout delamination contours of GFRP, CFRP, and AFRP plies with stacking sequence QI-V under 10 J impact at the angle of 60°.

downward pressure on the test specimen, would enhance the correlation between the numerical and experimental results. Although the validation case showed a considerable accuracy of the numerical model, obtaining the material properties of GFRP, CFRP and AFRP through experimental testing rather than relying on calculations and literature would be beneficial in order to further improve the accuracy of the simulation result.

Disclosure statement

No potential conflict of interest was reported by the authors.

References

[1] D.K. Hale, The physical properties of composite materials, J. Mater Sci., vol. 11, no. 11, pp. 2105–2141, 1976. DOI: 10.1007/BF02403361.
[2] B. Castanie, C. Bouvet, and M. Ginot, Review of composite sandwich structure in aeronautic applications, Compos. C Open Access., vol. 1, pp. 100004, 2020. DOI: 10.1016/j.jcomc.2020.100004.
[3] M.S. Sarfraz, H. Hong, and S.S. Kim, Recent developments in the manufacturing technologies of composite components and their cost-effectiveness in the automotive industry: a review study, Compos. Struct., vol. 266, pp. 113864, 2021. DOI: 10.1016/j.compstruct.2021.113864.
[4] F. Rubino, A. Nisticò, F. Tucci, and P. Carlone, Marine application of fiber reinforced composites: a review, JMSE., vol. 8, no. 1, pp. 26, 2020. DOI: 10.3390/jmse8010026.
[5] D.S. Vijayan, A. Sivasuriyan, P. Devarajan, A. Stefańska, Ł. Wodzyński, and E. Koda, Carbon fibre-reinforced polymer (CFRP) composites in civil engineering application—A comprehensive review, Buildings., vol. 13, no. 6, pp. 1509, 2023. DOI: 10.3390/buildings13061509.
[6] H.E.L. Etri, M.Z. Polat, and E.B. Özyılmaz, Classification, applications, and impact behavior of composite materials: a review, Mech. Adv. Mater. Struct., vol. 31, no. 30, pp. 12592–12635, 2024. DOI: 10.1080/15376494.2024.2326665.
[7] Y. Yang, Z. Miao, Y. Liu, H. Tu, and Y. Wei, A comprehensive review of fiber-reinforced polymer-matrix composites under low-velocity impact, Mech. Adv. Mater. Struct., pp. 1–39, 2025. DOI: 10.1080/15376494.2025.2458772.
[8] T. Ouyang, W. Sun, R. Bao, and R. Tan, Effects of matrix cracks on delamination of composite laminates subjected to low-velocity impact, Compos. Struct., vol. 262, pp. 113354, 2021. DOI: 10.1016/j.compstruct.2020.113354.
[9] X. Gong, X. Cheng, Q. Zhuang, Y. Cheng, X. Guo, and W. Huang, Experimental and numerical investigation on low-velocity impact damage and parametric study of composite rotor blades, Mech. Adv. Mater. Struct., pp. 1–14, 2024. DOI: 10.1080/15376494.2024.2377814.
[10] C. Meola, and G.M. Carlomagno, Impact damage in GFRP: new insights with infrared thermography, Compos. Part A Appl. Sci. Manuf., vol. 41, no. 12, pp. 1839–1847, 2010. DOI: 10.1016/j.compositesa.2010.09.002.

[11] G.A.O. Davies, and X. Zhang, Impact damage prediction in carbon composite structures, Int. J. Impact. Eng., vol. 16, no. 1, pp. 149–170, 1995. DOI: 10.1016/0734-743X(94)00039-Y.

[12] L. Brown, S. Monir, M. Jones, N. Luhyna, R.J. Day, and Y. Vagapov, A review of impact drop testing of composite laminate plates, Proc. 15th IEEE Int. Conf. on Industry Applications, pp.1659–1664, 2023. DOI: 10.1109/INDUSCON58041.2023.10374667.

[13] D. Banhart, S. Monir, O. Durieux, R.J. Day, M. Jones, N. Luhyna, and Y. Vagapov, A review of experimental and numerical methodologies for impact testing of composite materials, Sens. Technol., vol. 2, no. 1, pp. 2304886, 2024. DOI: 10.1080/28361466.2024.2304886.

[14] A.S. Alomari, K.S. Al-Athel, A.F.M. Arif, and F.A. Al-Sulaiman, Experimental and computational analysis of low-velocity impact on carbon-, glass- and mixed-fiber composite plates, J. Compos. Sci., vol. 4, no. 4, pp. 148, 2020. DOI: 10.3390/jcs4040148.

[15] A. Gliszczynski, Numerical and experimental investigations of the low velocity impact in GFRP plates, Compos. B Eng., vol. 138, pp. 181–193, 2018. DOI: 10.1016/j.compositesb.2017.11.039.

[16] A. Gonzalez-Jimenez, A. Manes, A. Beligni, M. Dziendzikowski, C. Sbarufatti, and M. Giglio, Modelling and experimental testing of thick CFRP composites subjected to low velocity impacts, Procedia Struct. Integr., vol. 24, pp. 101–109, 2019. DOI: 10.1016/j.prostr.2020.02.009.

[17] G. Perillo, N.P. Vedivik, and A.T. Echtermeyer, Damage development in stitch bonded GFRP composite plates under low velocity impact: experimental and numerical results, J. Compos. Mater., vol. 49, no. 5, pp. 601–615, 2015. DOI: 10.1177/0021998314521474.

[18] A.J. McMillan, C. Monroy Aceves, and M.P.F. Sutcliffe, Moderate energy impact analysis combining phenomenological contact law with localised damage and integral equation method, Int. J. Impact. Eng., vol. 43, pp. 29–39, 2012. DOI: 10.1016/j.ijimpeng.2011.11.008.

[19] A.J. McMillan, M.I. Darby, B.C. Jones, and G.R. Evans, Calculation of forces due to transverse impact of damped polycrystalline graphite beams, Carbon., vol. 34, no. 1, pp. 121–125, 1996. DOI: 10.1016/0008-6223(95)00152-2.

[20] M.O. Bozkurt, L. Parnas, and D. Coker, Simulation of drop-weight impact test on composite laminates using finite element method, Procedia Struct. Integr., vol. 21, pp. 206–214, 2019. DOI: 10.1016/j.prostr.2019.12.103.

[21] Y. Zhao, and X. Zhou, Numerical analysis of unidirectional carbon-fibre/epoxy composite laminates under low velocity impacts of different forms, Comput. Mater. Sci., vol. 231, pp. 112611, 2024. DOI: 10.1016/j.commatsci.2023.112611.

[22] Y. Mao, L. Hong, S. Ai, H. Fu, and C. Chen, Dynamic response and damage analysis of fiber-reinforced composite laminated plates under low-velocity oblique impact, Nonlinear Dyn., vol. 87, no. 3, pp. 1511–1530, 2017. DOI: 10.1007/s11071-016-3130-5.

[23] Z. Li, J. Zhang, B. Lu, X. Zhao, J. Wang, and N. Yang, Damage mechanisms and analytical model of CFRP laminate under low-velocity normal and oblique impacts, Int. J. Crashworthiness., vol. 29, no. 3, pp. 430–444, 2024. DOI: 10.1080/13588265.2023.2258626.

[24] Y. Zhang, Z. Gong, E. Pan, and C. Zhang, A novel solution of rectangular composite laminates under oblique low-velocity impacts, Appl. Math. Mech. Engl. Ed., vol. 45, no. 12, pp. 2165–2182, 2024. DOI: 10.1007/s10483-024-3199-6.

[25] P. Rawat, N.K. Singh, K.K. Singh, and N. Agrhari, Influence of oblique impact on glass fiber-reinforced polymer composites: a numerical approach. In: Trends in Materials Engineering. Lecture Notes on Multidisciplinary Industrial Engineering, I. Singh, P. Bajpai, and K. Panwar, Eds. Springer, Singapore, pp. 77–86, 2019.

[26] J. Sun, L. Huang, and J. Zhao, Oblique low-velocity impact response and damage behavior of carbon-epoxy composite laminates, Materials., vol. 15, no. 15, pp. 5256, 2022. DOI: 10.3390/ma15155256.

[27] O. Falcó, C.S. Lopes, D.E. Sommer, D. Thomson, R.L. Ávila, and B.H.A.H. Tijs, Experimental analysis and simulation of low-velocity impact damage of composite laminates, Compos. Struct., vol. 287, pp. 115278, 2022. DOI: 10.1016/j.compstruct.2022.115278.

[28] ASTM International. Standard Test Method for Measuring the Damage Resistance of a Fiber-Reinforced Polymer Matrix Composite to a Drop-Weight Impact Event, ASTM International, West Conshohocken, PA, 2014.

[29] Y. Luo, Improved Voigt and Reuss formulas with the Poisson effect, Materials., vol. 15, no. 16, pp. 5656, 2022. DOI: 10.3390/ma15165656.

[30] E. Egorikhina, S.V. Bogovalov, and I.V. Tronin, Determination of mechanical characteristics of unidirectional fiber composites, Phys. Procedia., vol. 72, pp. 66–72, 2015. DOI: 10.1016/j.phpro.2015.09.021.

[31] J. Echaabi, F. Trochu, and R. Gauvin, Review of failure criteria of fibrous composite materials, Polym. Compos., vol. 17, no. 6, pp. 786–798, 1996. DOI: 10.1002/pc.10671.

[32] F. Paris, A Study of Failure Criteria of Fibrous Composite Materials, NASA, Hampton, VA, 2001.

[33] ANSYS. ANSYS Composite PrepPost User's Guide, ANSYS, Canonsburg, PA, 2015.

[34] Y. Xing, W. Xu, and V. Buratti, The correlation and determination matrices associated with the burst design of a subsea carbonfibre-epoxy composite flow-line, IOP Conf. Ser: mater. Sci. Eng., vol. 700, pp. 012021, 2019. DOI: 10.1088/1757-899X/700/1/012021.

[35] V. Mahesh, S. Joladarashi, and S.M. Kulkarni, A comprehensive review on material selection for polymer matrix composites subjected to impact load, Def. Technol., vol. 17, no. 1, pp. 257–277, 2021. DOI: 10.1016/j.dt.2020.04.002.

[36] AGY. High Strength Glass Fibers – An Overview of Glass Fiber Technology, AGY, Aiken, CA, 2021.

[37] TORAYCA. T700S Data Sheet, Toray Composite Materials America, Santa Ana, CA, 2002.

[38] DuPont. Kevlar Aramid Fiber Technical Guide, DuPont, Richmond, VA, 2017.

[39] L. Liu, S. Gao, Z. Jiang, Y. Zhang, D. Gui, and S. Zhang, Amide-functionalized ionic liquids as curing agents for epoxy resin: preparation, characterization, and curing behaviors with TDE-85, Ind. Eng. Chem. Res., vol. 58, no. 31, pp. 14088–14097, 2019. DOI: 10.1021/acs.iecr.9b01888.

[40] M.B. Moketla, and M. Shukla, Design and finite element analysis of FRP LPG cylinder, Int. J. Instrum. Control. Autom., vol. 2, no. 1, pp. 44–47, 2012. DOI: 10.47893/IJICA.2012.1066.

[41] P.R. Lakshmi, and P.R. Reddy, Investigation of interlaminar shear strength in carbon epoxy and carbon epoxy carbon nanotubes using experimental and finite element technique, Int. J. Eng. Res. Appl., vol. 2, no. 3, pp. 1–10, 2012.

[42] Y. Qu, Y. Zhang, and J. Qu, Micro-driving behavior of carbon-fiber-reinforced epoxy resin for standing-wave ultrasonic motor, Polym. Compos., vol. 37, no. 7, pp. 2152–2159, 2015. DOI: 10.1002/pc.23394.

[43] T.W. Clyne, and D. Hull, An Introduction to Composite Materials, 3rd ed. Cambridge University Press, Cambridge, 2019.

[44] A. Puck, J. Kopp, and M. Knops, Guidelines for the determination of the parameters in Puck's action plane strength criterion, Compos. Sci. Technol., vol. 62, no. 3, pp. 371–378, 2002. DOI: 10.1016/S0266-3538(01)00202-0.

[45] A. Pai, R. Suri, A.K. Bhave, P. Verma, and P. N H, Puck's criterion for the tensile response of composite laminates: A numerical approach, Adv. Eng. Softw., vol. 175, pp. 103364, 2023. DOI: 10.1016/j.advengsoft.2022.103364.

[46] Y. Zhao, S. Yan, and J. Jia, Fabrication and statics performance of pyramidal lattice stitched foam sandwich composites,

Comput. Model. Eng. Sci., vol. 126, no. 3, pp. 1251–1274, 2021. DOI: 10.32604/cmes.2021.013478.

[47] I.M. Daniel, and O. Ishai, Engineering Mechanics of Composite Materials, 2nd ed., Oxford University Press, Oxford, 2006.

[48] C. Schuecker, and H.E. Pettermann, A continuum damage model for fiber reinforced laminates based on ply failure mechanisms, Compos. Struct., vol. 76, no. 1-2, pp. 162–173, 2006. DOI: 10.1016/j.compstruct.2006.06.023.

[49] H. Saghafi, G. Minak, and A. Zucchelli, Effect of preload on the impact response of curved composite panels, Compos. B Eng., vol. 60, pp. 74–81, 2014. DOI: 10.1016/j.compositesb.2013.12.026.

[50] B.M. Fadhil, Effect of plies stacking sequence and tube geometry on the crush behavior of tube under low velocity impact - numerical study, Int. J. Mech. Appl., vol. 3, no. 2, pp. 44–51, 2013. DOI: 10.5923/j.mechanics.20130302.02.

[51] F. Wang, J. Ding, and Z. Chen, Statistical analysis of the progressive failure behavior for fiber-reinforced polymer composites under tensile loading, Polymers., vol. 6, no. 1, pp. 145–159, 2014. DOI: 10.3390/polym6010145.

[52] L. Russell, and A. Goodman, Performance Composites. Mechanical Properties of Carbon Fibre Composite Materials. [Online]. http://www.performance-composites.com/carbonfibre/mechanicalproperties_2.asp

[53] G.H. Staab, Laminar Composites, 2nd ed. Elsevier, Oxford, 2015.

[54] Assessment of Research Needs for Wind Turbine Rotor Materials Technology, National Academy Press, Washington, DC, 1991.

[55] Otai Special Steel, H13 Tool Steel. [Online]. Available: https://www.astmsteel.com/product/h13-tool-steel-x40crmov5-1-skd61-hotwork-steel

[56] J.S. Sun, K.H. Lee, and H.P. Lee, Comparison of implicit and explicit finite element methods for dynamic problems, J. Mater. Process. Technol., vol. 105, no. 1-2, pp. 110–118, 2000. DOI: 10.1016/S0924-0136(00)00580-X.

[57] ANSYS. Workshop 3.1 FEA: Global Mesh Controls, ANSYS, Canonsburg, PA, 2019.

[58] ANSYS. Module 05: Mesh Quality, ANSYS, Canonsburg, PA, pp. 14–15, 2019.